A Diagnostic Analysis of the Superstorm of March 1993

ZONGHUI HUO, DA-LIN ZHANG, AND JOHN GYAKUM

Department of Atmospheric and Oceanic Sciences, McGill University, Montreal, Quebec, Canada

ANDREW STANIFORTH

Recherche en prévision numérique, Atmospheric Environment Service, Dorval, Quebec, Canada

(Manuscript received 11 April 1994, in final form 4 August 1994)

ABSTRACT

In this study, the synoptic evolution of the March 1993 superstorm is documented using conventional observations, and the predictability and deepening mechanisms of the storm are investigated using a newly implemented mesoscale version of the Canadian Regional Finite-Element (RFE) Model. It is found that although the RFE model can predict well the large-scale background flow associated with the storm, it fails to predict various important mesoscale elements when it is initialized with fields that contain weak signals of the low-level circulations. However, when the storm is located close to the data-rich region, the model has considerable skill in predicting those mesoscale elements, such as a prefrontal squall line, upper- and low-level jets, as well as the quantitative aspects of their associated precipitation.

Observational analysis reveals that the storm developed in a convectively unstable prestorm environment with ample moisture content. It first experienced an antecedent surface vorticity growth over the anomalously warm water of the Gulf of Mexico mainly through condensation processes. Then the storm deepened rapidly as two midlevel short-wave troughs approached, merged, and interacted with a thermally direct ageostrophic circulation in the entrance region of an upper-level jet streak. A potential vorticity (PV) diagnosis reveals that the intensification of the midlevel troughs is related to the pronounced descent of stratospheric PV-rich air associated with tropopause depressions. It is found that the tropopause depression, latent heat release, weak static stability, the jet streak–induced ageostrophic circulation, and surface sensible and latent heat fluxes, act together to determine the amplification and evolution of the storm, although their relative importance differs at different stages of the storm's development. In particular, latent heat release accounts for roughly 40% of the total deepening, and the heating-induced ageostrophic circulations provide an important coupling of the surface cyclogenesis with the above-mentioned processes.

1. Introduction

The superstorm of 12–14 March 1993 developed rapidly from a surface low pressure system over the northern Gulf of Mexico. As it moved northeastward along the eastern seaboard, the storm broke snowfall, rainfall, and low pressure records. The superstorm caused widespread damage to the Cuban sugar crop, and produced tornadoes in Florida and hurricane-force winds and damaging tides along the Atlantic coast. Storm-related casualties and missing at sea totaled more than 290, and property damage well exceeded $1 billion. Although the net 30-hPa central pressure fall during the 24-h period beginning at 0000 UTC 13 March qualifies it as only a weak "bomb" according to Sanders and Gyakum (1980), the severe weather conditions associated with it were substantially stronger than those of some moderate and even strong oceanic "bombs." Because of its explosively deepening nature and record breakings, this storm has been named "the storm of the century" and has received considerable attention.

There have been numerous case studies of explosively deepening cyclones since the first climatological study of "bombs" by Sanders and Gyakum (1980). They include the Presidents' Day cyclone of February 1979 (Bosart 1981; Bosart and Lin 1984; Uccellini et al. 1984, 1985, 1987; Whitaker et al. 1988), the *Queen Elizabeth II* cyclone of September 1978 (Gyakum 1983a,b; Anthes et al. 1983; Uccellini 1986), the eastern Pacific cyclone of November 1981 (Reed and Albright 1986; Kuo and Reed 1988), as well as some interesting storms that occurred during the Genesis of Atlantic Lows Experiment (GALE, see Wash et al. 1990), the Experiment on Rapidly Intensifying Cyclones over the Atlantic (ERICA, see Reed et al. 1993; Roebber 1993; Roebber et al. 1994), and the Canadian Atlantic Storms Program (CASP, see Mailhot and Chouinard 1989). These studies have focused on a va-

Corresponding author address: Zonghui Huo, Department of Atmospheric and Oceanic Sciences, McGill University, 805 Sherbrook St. W., Montreal, PQ H3A 2K6, Canada.

© 1995 American Meteorological Society

riety of structural entities and physical processes as necessary ingredients for explosive cyclogenesis, such as the presence of strong baroclinicity, short-wave troughs, stratospheric extrusions, upper-level jet streaks and low-level jets, symmetric instability and weak static stability, latent heat release, and surface sensible and latent heat fluxes. These upper- and low-level elements are often dynamically coupled through vertical ageostrophic circulations that are aided by upright or slantwise convection.

With the extensive research and technological improvements in the past few years, there have been marked improvements in the model predictability of explosively deepening cyclones (Sanders 1987; Sanders and Auciello 1989). However, the level of model performance is inconsistent, and often characterized by considerable case-to-case variability (Kuo and Low-Nam 1990) and even model-to-model and run-to-run variability (Roebber 1990). These inconsistencies are attributable to the use of imperfect initial conditions, poor grid resolution, or improper model physics representations. Such inconsistencies also occurred in the numerical prediction of "the storm of the century," although it was reasonably predicted several days in advance by operational models at both the Canadian Meteorological Centre (CMC) and the U.S. National Meteorological Center (NMC).

The purposes of this study are to (i) document the development and evolution; (ii) investigate the model predictability; and (iii) examine the possible mechanisms leading to the explosive deepening of the superstorm using both the conventional observations and the CMC operational Regional Finite-Element (RFE) Model. The presentation of the results is organized as follows. Section 2 provides a synoptic overview of the large-scale background conditions associated with the development of the superstorm. Section 3 describes briefly the major features of the RFE model used for the present study. Section 4 discusses the predictability of the superstorm by the operational RFE model when it is initialized at different times. Section 5 shows verification of the control prediction against available observations. The importance of various possible dynamical and physical processes in the explosive cyclogenesis is examined in section 6. A summary and concluding remarks are given in the final section.

2. Synoptic overview

The superstorm appeared first as a surface low in northern Mexico around 1200 UTC 11 March 1993, with a weak 500-hPa short-wave trough approaching from the west. Further to the west, there was another midlevel short-wave trough that was amplifying as it moved toward the Rockies. By 1200 UTC 12 March, the surface low has moved offshore over the anomalously warm water of the northwestern Gulf of Mexico [the sea surface temperature is more than 3°C above the monthly normal, Gilhousen (1994)], followed by a strong cold-air surge from the north. The low pressure system began its initial development in a strong baroclinic zone between the continental air mass and the marine air mass over the warm "Eddy Vasquez" (Walker 1993) in the northwestern Gulf of Mexico. Then, the storm experienced further development as it moved northeastward and entered into another baroclinic zone with a strong sea surface temperature (SST) gradient to the south of the Mississippi River delta.

Figures 1–4 show the CMC regional analysis maps (except that Fig. 1a is manually modified to fit the surface observations) for the period of 1200 UTC 12 March–1200 UTC 14 March 1993, which covers roughly the life cycle of the storm. A portion of the geostationary satellite and composite radar imagery associated with the superstorm is given in Fig. 5. At 1200 UTC 12 March, the cyclone center was located to the northeast of Brownsville with a mean sea level pressure (MSLP) of 1002 hPa (Fig. 1a). On the 850-hPa map, weak warm advection prevailed in a wide area of southerly flow ahead of the surface low, while a cold air mass with strong temperature gradients was advected southward to the east of the Rockies, leading to a rapid increase of the baroclinicity along the southern seaboard (Fig. 1b). The presence of the strong southerly flow is indicative of ample moisture content being transported into the baroclinic zone for subsequent latent heat release. The midtroposphere was characterized by two short-wave troughs, each associated with an amplifying vorticity center (Fig. 1c). The surface cyclone was located over an area of positive vorticity advection ahead of the upper-level troughs (cf. Figs. 1a,c). The southeastern trough appeared to be the primary midlevel forcing for the initial development of the cyclone, whereas the northwestern one was responsible for the explosive deepening at a later stage. The upper troposphere exhibited a "double-jet" structure—that is, one ahead of and the other behind the upper-level trough—they are denoted by "A" and "B," respectively, in Fig. 1d. The double-jet structure has been also noted by Bell and Bosart (1993) and others in the study of the effect of tropopause depression on extratropical cyclogenesis. Note that the westerly jet has intensified rapidly in response to the enhanced baroclinicity to the south. The presence of such strong jet streaks is an indication of strong baroclinicity, which would determine the subsequent explosive deepening of the storm.

At 0000 UTC 13 March, the cyclone had just experienced a rapid development over the warm ocean as the low center moved to approximately 150 km south of New Orleans with a MSLP of 992 hPa (Fig. 2a). It should be noted that this value is higher than the analyzed 989 hPa quoted by Gilhousen (1994), or the 984 hPa stated by Uccellini et al. (1994). This higher value is due to missing observations in the Regional Data Assimilation System. A close to hurricane-force wind of 30 m s^{-1} was observed to the southwest of the cy-

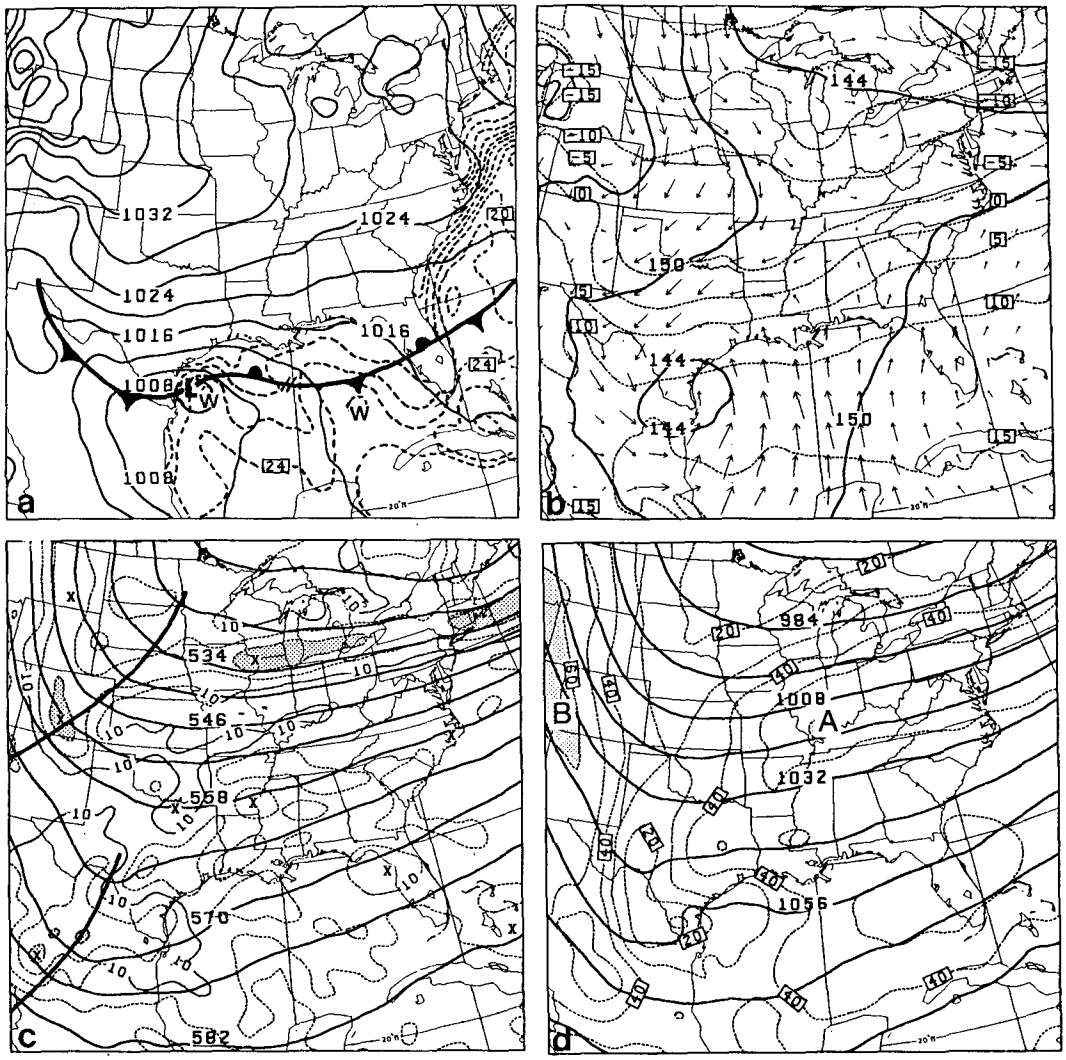

FIG. 1. Observational analysis at 1200 UTC 12 March 1993. (a) Mean sea level pressure (MSLP) at intervals of 4 hPa and sea surface temperature (dashed) at intervals of 2°C; subjectively analyzed fronts are also shown. (b) The 850-hPa geopotential height (solid) at intervals of 6 dam and temperature (dashed) at intervals of 5°C, superposed with wind vectors. (c) The 500-hPa geopotential height (solid) at intervals of 6 dam and absolute vorticity (dashed) at intervals of 5×10^{-5} s^{-1}. Shading denotes absolute vorticity larger than 20×10^{-5} s^{-1}, and thick solid lines represent the subjectivity determined trough lines. (d) The 250-hPa geopotential height (solid) at intervals of 12 dam and isotachs (dashed) at intervals of 10 m s^{-1}. Shading denotes the central portion of jet streaks, as indicated by "A" and "B."

clone center. The surface cold front has also intensified rapidly during the 12-h period and has now moved into the central Gulf of Mexico. Meanwhile, the quasi-stationary front to the east began to move northward as a warm front under the influence of the low-level southerly flow. Low-level temperature analysis (not shown) indicates that weak coastal frontogenesis and cold-air damming occurred to the east of the Appalachians, and these signals can also be seen from Fig. 2a as a weak trough off the coast and a weak ridge west of the coastal line. The satellite imagery at this time showed a comma-shaped pattern of cloudiness associated with the cyclone with a well-developed squall line occurring ahead of the cold front (Fig. 5a). Meanwhile, the radar summary (Fig. 5d) displayed an extensive area of precipitation over the southeastern United States and adjacent waters that was partly associated with the northern part of the prefrontal squall line, and a large area of less-organized precipitation over the eastern United States that was associated with the warm front. The cloud tops near the storm center reached 28 000 ft (8.5 km) and some cloud tops at the eastern tip of the warm front went up to 34 000 ft (10.5 km). At 850 hPa (Fig. 2b), the cyclonic flow intensified. A low-level jet developed ahead of the prefrontal squall line. This southerly jet is a part of the warm conveyor belt that helps

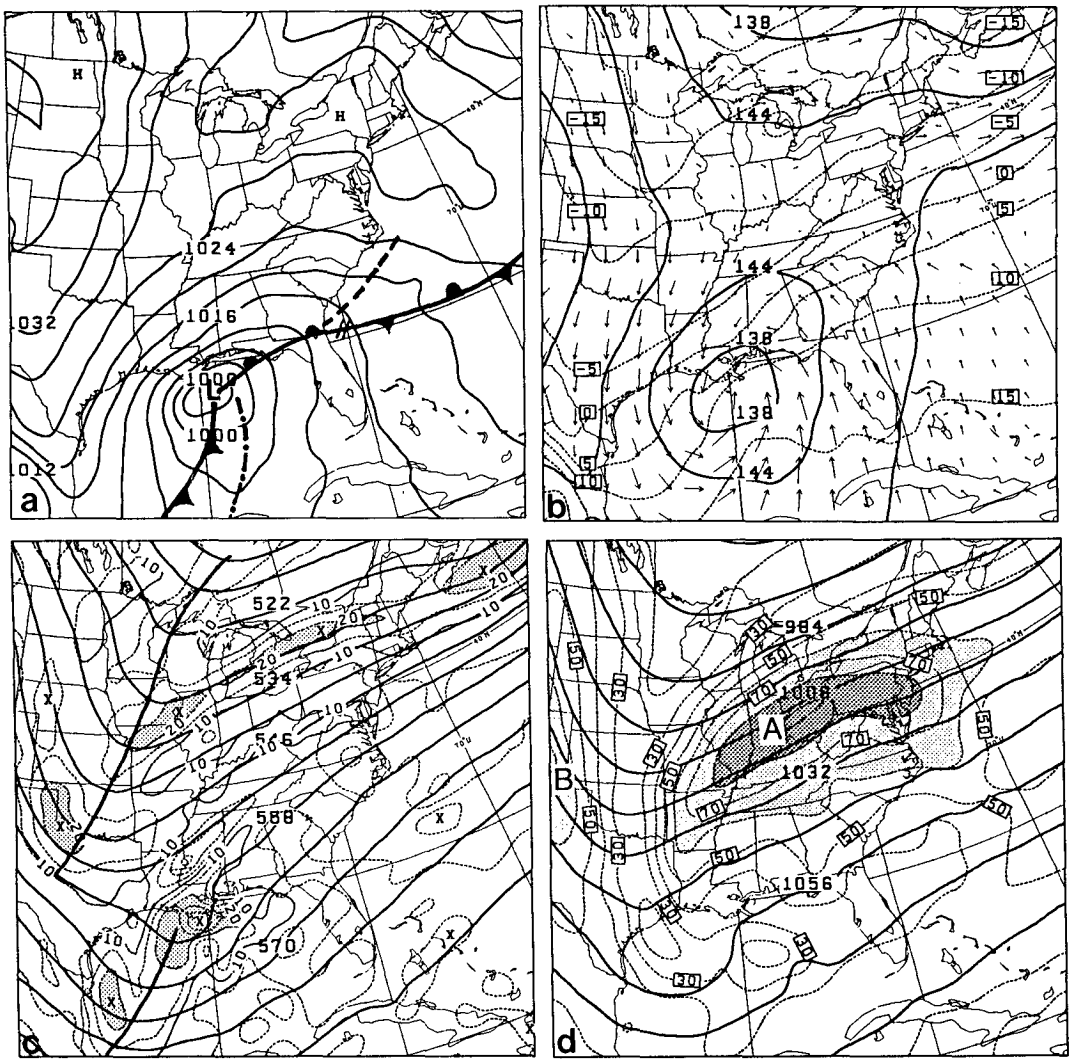

FIG. 2. As in Fig. 1 but for 0000 UTC 13 March 1993.

transport warm and moist air from the ocean to the south toward the warm frontal zone and the cyclone center (Carlson 1980). This low-level transport of warm and moist air tends to convectively destabilize the prestorm environment in the warm sector and to generate a more favorable condition for the intensification of the prefrontal squall system and stratiform precipitation near the cyclone center. Moreover, the warm moist advection ahead of the cold front (due to the low-level jet) and the strong cold advection behind the cold front would also increase the cross-front baroclinicity. At 500 hPa (Fig. 2c), both short-wave troughs were intensifying and their associated vorticity maxima were increasing. Note that the eastern trough had moved close to the center of the surface low; so its positive vorticity advection toward the low appears to have played an important role in the initial development of the cyclone. At 250 hPa (Fig. 2d), the westerly jet (i.e., A) had intensified rapidly from 60 to 90 m s^{-1} during the previous 12-h period; the northwesterly jet (i.e., B) had also intensified somewhat. Note also that the surface cyclone was now located beneath the right entrance region of the jet streak A, a position that is favorable for surface cyclogenesis according to Uccellini and Johnson (1979).

Because of the above-mentioned favorable large-scale conditions, the storm deepened more than 30 hPa during the next 24 h as it moved northeastward along the east seaboard. At 1200 UTC 13 March, the surface low was in central Georgia with a MSLP of 973 hPa (Fig. 3a). The warm front, that was approximately parallel to the east coast, had been strengthened markedly. The prefrontal squall line had swept across Florida (Fig. 5b) and spawned about 25 tornadoes. It had also left behind an extensive area of low-level cumulus clouds or streamers over the warm water of the Gulf of

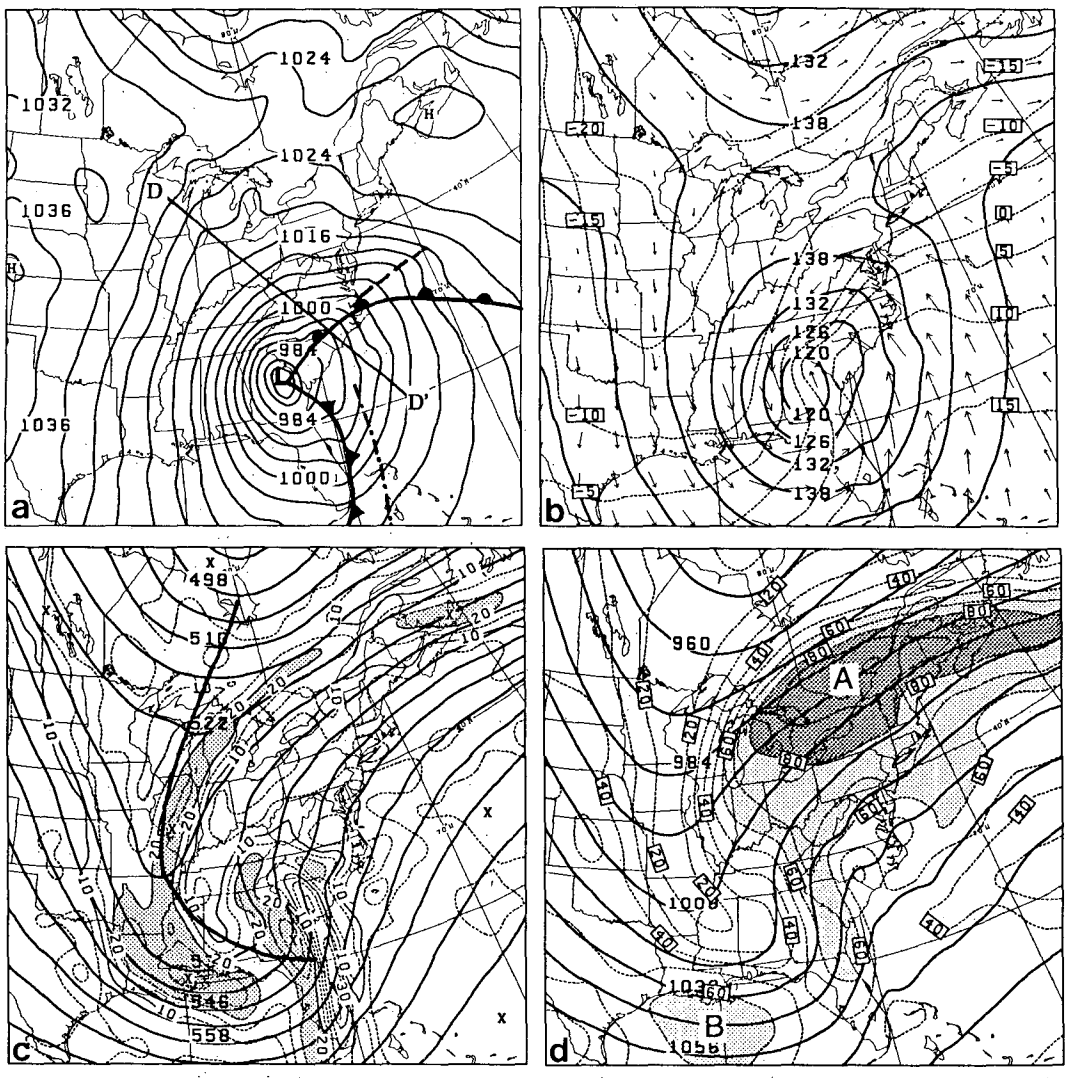

FIG. 3. As in Fig. 1 but for 1200 UTC 13 March 1993. Line *DD'* in (a) shows the location of the cross section used in Fig. 16.

Mexico. Thunder and lightning were still observed at this time along the squall line and near the cyclone center. A dry slot, nearly cloud-free, was wrapped around into the cyclone center (Figs. 5b,e). Six hours later (Figs. 5c, f), the southern part of the squall line began to dissipate, whereas its northern portion became more convectively active, particularly to the east of the cyclone center, where thunder and lightning were also reported. The 850-hPa map (Fig. 3b) was similar to that 12 h earlier, but the low-level jet had increased in strength; it implied again the significant moisture transport from the tropical ocean into the warm sector of the cyclone. At 500 hPa (Fig. 3c), the two short-wave troughs began to merge and produced a negative tilt. The vorticity centers associated with the two respective troughs had intensified substantially; they eventually merged into one vorticity band (Fig. 4c). The westerly jet streak (i.e., A) had strengthened by another 10 m s^{-1} as it progressed northeastward, while the northwesterly jet streak (i.e., B) had plunged to the base of the upper-level trough (Fig. 3d). Thus, the surface cyclone was now situated at the right entrance of the northern jet "A" and the left exit region of the southern jet "B," which was in a more favorable position for cyclogenesis, according to Uccellini and Kocin (1987).

By 0000 UTC 14 March, the central MSLP had deepened to 966 hPa. But the storm had entered its occlusion stage (Fig. 4a), and it began slowly filling a few hours later. The prefrontal squall line dissipated gradually as it moved into a convectively less unstable environment. However, corresponding to the strongest stage of the cyclone, the mid- and upper-level disturbances reached their maximum intensity. For example, a closed low pressure area with increased cyclonic vorticity appeared at 500 hPa

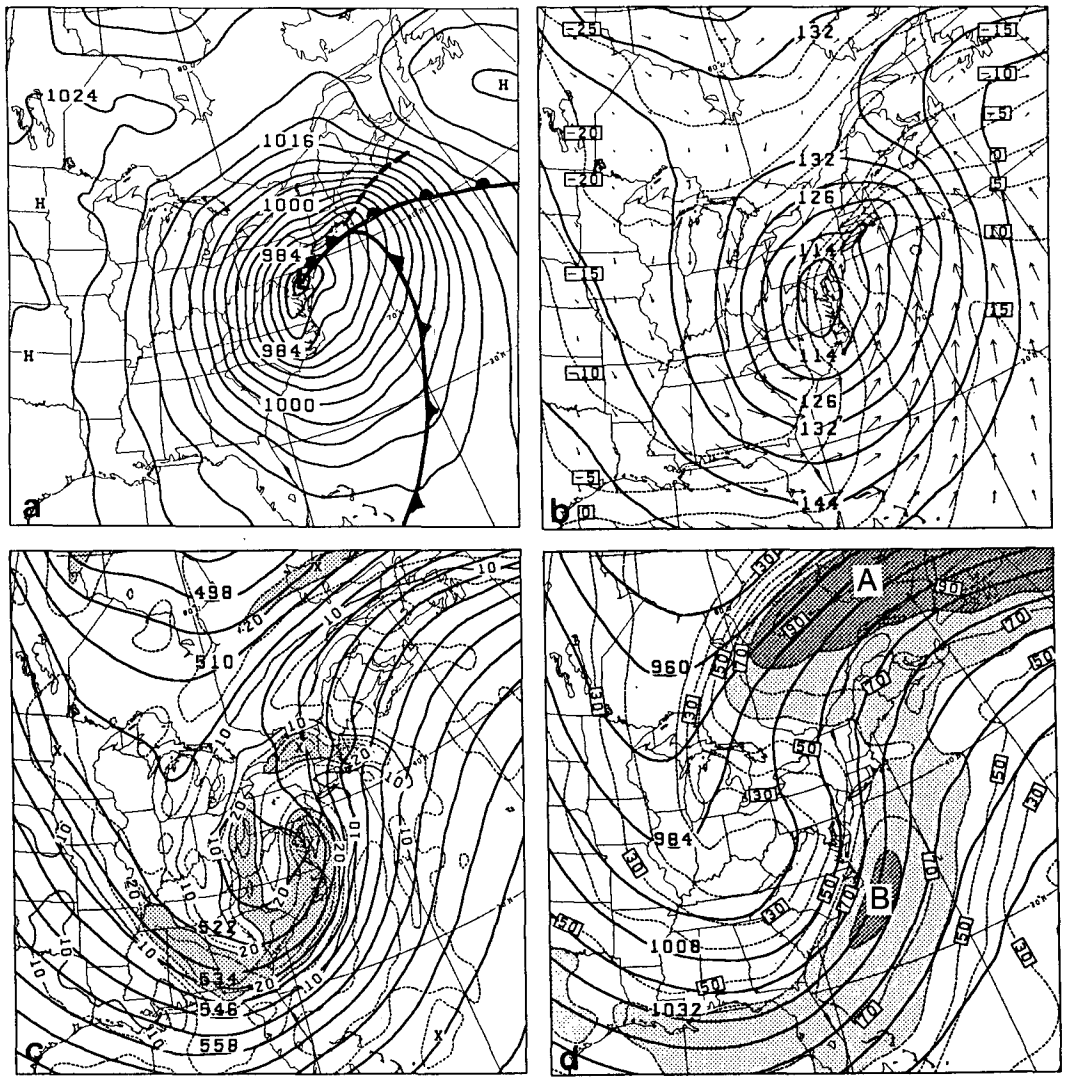

FIG. 4. As in Fig. 1 but for 0000 UTC 14 March 1993.

as the two short-wave troughs merged (Fig. 4c). At 250 hPa, the above-mentioned two jet streaks intensified further and the associated strong winds occurred over a more extensive region. Afterward, the storm moved northeastward and experienced another short period of redevelopment in the coastal region of the Labrador Sea, and then filled gradually.

In summary, this superstorm began as a weak surface low in northern Mexico. Then, it developed rapidly over the anomalously warm Gulf of Mexico, and deepened explosively as two midlevel short-wave troughs approached and merged. Along its path to the Gulf of St. Lawrence, the storm dropped a considerable amount of both convective and stratiform precipitation. Since ageostrophic processes are often responsible for conversion of available potential energy to kinetic energy during rapid cyclogenesis and since they can be significant at small scales, it is advantageous to use a high-resolution model prediction of the superstorm to better examine the relationships between the surface cyclone and various mid- and upper-level disturbances, and to investigate the dynamical processes leading to the explosive cyclogenesis. In addition, the model predictability of the storm will be studied to gain insight into the variability of the model performance when it is initialized at different times.

3. Numerical prediction system

a. The RFE model

To provide a high-resolution and more realistic four-dimensional dataset for studying the deepening mechanisms associated with the superstorm, a newly imple-

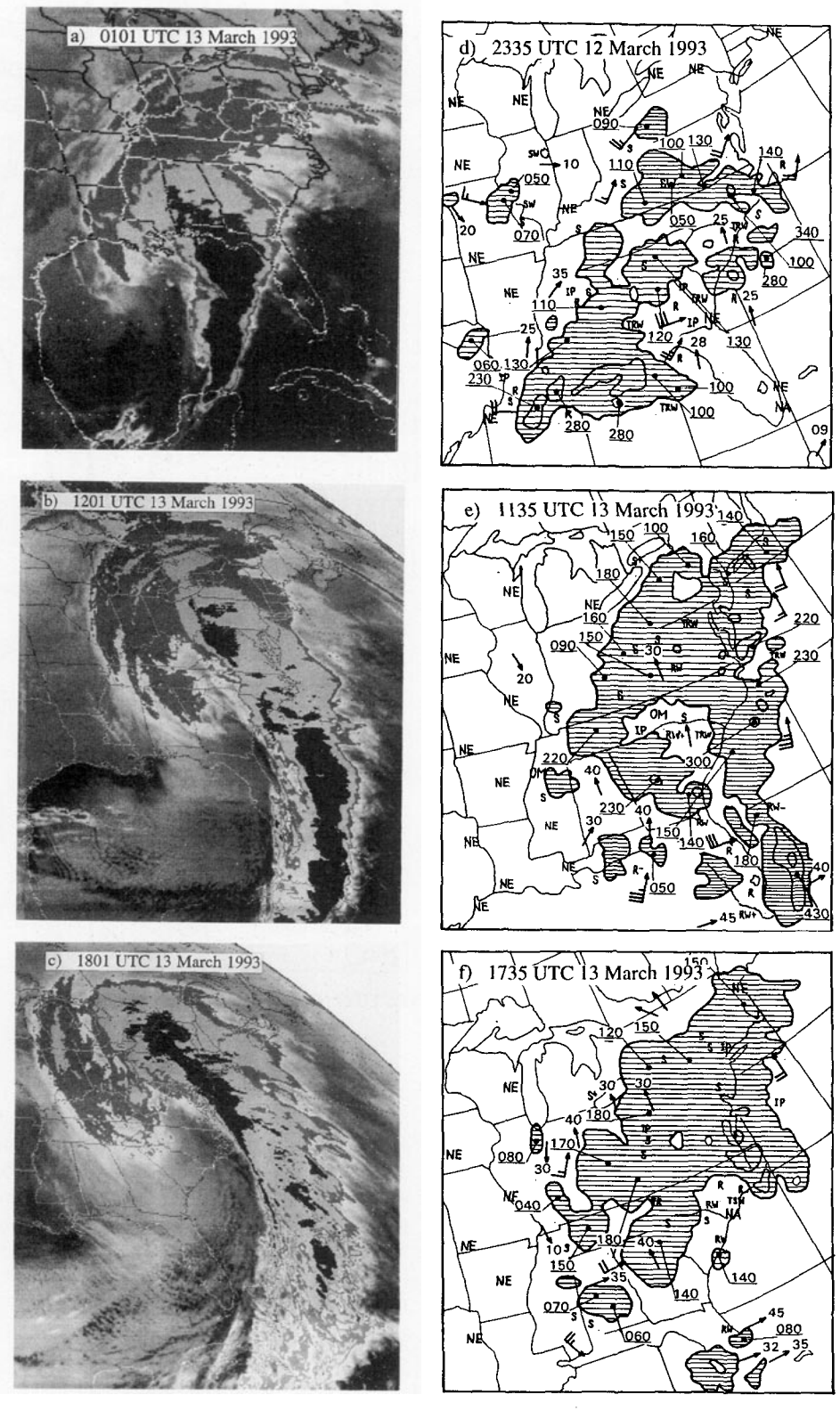

FIG. 5. The left panels show the enhanced infrared geostationary satellite imagery at (a) 0101 UTC, (b) 1201 UTC, and (c) 1801 UTC 13 March 1993. The right panels show the composite radar imagery at (d) 2335 UTC 12 March, (e) 1135 UTC, and (f) 1735 UTC 13 March 1993.

mented mesoscale version of the RFE model is used for the present study. Its major improvements over the old version of the RFE model include (i) a grid size of 50 km instead of 100 km in the uniform-resolution region of the variable grid, and (ii) a Kuo (1974)–type convective parameterization scheme replaces the Manabe moist adjustment scheme to handle subgrid-scale moist convection. A supersaturation removal scheme is employed to compute grid-scale condensation.

In this model, the hydrostatic primitive equations in σ coordinates (23 levels in the present case) are integrated using a semi-implicit temporal discretization and a finite-element spatial discretization. The computational domain covers the entire Northern Hemisphere that is overlaid on a polar-stereographic map projection true at 60°N, with boundaries tangent to the equator. The 50-km uniform-resolution subdomain almost covers the analysis domain shown in Figs. 1–4 that is surrounded by a smoothly-varying mesh, in which the grid size increases by a constant factor until the equator is reached. Staniforth and Mitchell (1978) have shown the advantages of using the variable-resolution approach for regional-scale modeling. The solid-wall condition is imposed at all lateral boundaries. A semi-Lagrangian scheme (Tanguay et al. 1989) is used to treat horizontal and vertical advection terms, which allows the use of a large time step (600 s for the present study). A second-order horizontal diffusion is applied for temperature, vorticity, divergence, and specific humidity.

The other physics representations used for the present study include vertical turbulent fluxes of momentum, heat, and moisture, and solar and infrared radiation. The surface temperature and moisture are predicted by the force–restore method (Deardorf 1978). Surface-layer exchanges of heat, moisture, and momentum are treated according to similarity theory, assuming a stratified surface layer between ground and the first level. A turbulent kinetic energy–based boundary layer scheme (Mailhot and Benoit 1982; Benoit et al. 1989) is utilized to treat the vertical turbulent transport in the planetary boundary layer (PBL).

b. Initialization

Accurate specification of the initial mass and wind fields is crucial for obtaining a high quality forecast. To obtain improved initial conditions with fewer precipitation spinup problems, the model is initialized using a recently implemented regional data assimilation system (RDAS) at CMC (Chouinard et al. 1994). The RDAS is performed by maximizing the coherence between the RFE model and the data assimilation cycle. Its operational procedure commences 12 h earlier (t_0 − 12 h) from the initial time with a trial field produced by interpolating a 6-h global model forecast initialized at t_0 − 18 h to the RFE model grid. The trial field is then enhanced by observations at t_0 − 12 h, followed by two 6-h initialization–forecast–analysis cycles. The output of the last analysis is fed directly into the RFE model for integration.

4. Model predictability

To examine to what extent the CMC operational model can succeed in predicting the various meteorological elements associated with the superstorm, the recently implemented (November 1993) 50-km-resolution mesoscale version of the RFE model is rerun at the following four different initialization times: (i) 0000 UTC 12 March (i.e., 12 h prior to the incipient stage, when the cyclone was located over the Mexican Plateau); (ii) 1200 UTC 12 March (i.e., the beginning of the incipient stage, when the cyclone moved over the warm water of the Gulf of Mexico); (iii) 0000 UTC 13 March (i.e., the beginning of the most rapid deepening stage, when the cyclone center moved close to the southern shore of the United States); and (iv) 1200 UTC 13 March (i.e., half-way into the rapid-deepening period, when the cyclone was centered over central Georgia). All the test runs are then integrated to 0000 UTC 14 March when the superstorm reached its maximum intensity. The position and intensity of the prefrontal squall line and the surface cyclone are verified against observational analyses at 1200 UTC 13 and 0000 UTC 14 March 1993, respectively. For the purpose of the model verification, central MSLP is used here as a measure of the cyclone's intensity, although it does not always provide the most desirable indication of a cyclone's intensification.

It is clear from Fig. 6 that all test runs reproduce well the location of the cyclone's center, with an error varying between 100 and 200 km. Likewise, other large-scale structures, such as midlevel baroclinic waves and upper-level jet streaks are all reasonably reproduced, as compared to observational analysis. Thus, the predicted storm tracks, that are mainly determined by large-scale processes, are generally in good agreement with observations (not shown), although there is some degree of error in the position of the storm. These aspects of the forecast are quite remarkable, particularly for the 48-h prediction (see Fig. 6a) in which the storm's signal was very weak to begin with and it also was situated over a data-sparse region at the model initial time.

Of course, this by no means indicates that the model prediction is insensitive to the initial signals of the storm or to other details of the initial conditions. In fact, there is some variability in the forecasts of the storm's intensity and structure; the differences between the model forecasts and observational analyses are smaller when the model is initialized at later times—for example, after 0000 UTC 13 March. A comparison of Figs. 6 and 4 reveals that the integrations initialized at 0000 and 1200 UTC 13 March are in best agreement with the observations. The inte-

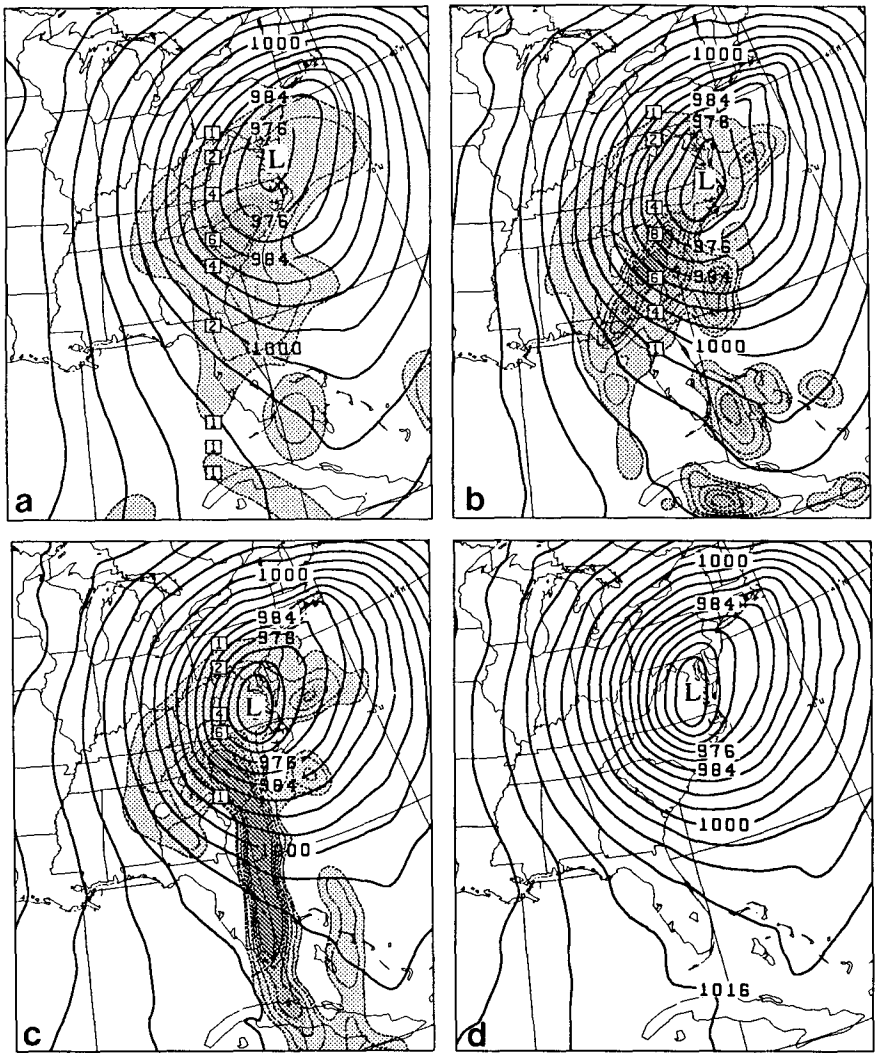

FIG. 6. Predicted mean sea level pressure at intervals of 4 hPa valid at 0000 UTC 14 March and hourly precipitation rates (mm h^{-1}) valid at 1200 UTC 13 March from (a) 48-h, (b) 36-h, (c) 24-h, and (d) 12-h integrations that are initialized at 0000 UTC 12 March, 1200 UTC 12 March, 0000 UTC 13 March, and 1200 UTC 13 March 1993, respectively.

grations initialized at 0000 and 1200 UTC 12 March, however, predict poorly the intensity of the storm; likewise, the RFE forecasts valid at earlier times (e.g., 1200 and 1800 UTC 12, and 0000 UTC 13 March) fail to reproduce the intensity of the storm. (Note that the central pressures and positions at 0000 and 1200 UTC 12 March in the CMC analysis differ slightly from the manually analyzed.) Of particular significance is that quantitative precipitation forecasts (QPFs) appear to be extremely sensitive to the quality of initial conditions. Owing to the imperfect initial fields, the model runs initialized at both 0000 and 1200 UTC 12 March fail to predict the development and propagation of the prefrontal squall line, and, therefore, the squall line associated precipitation. For example, both QPFs valid at 1200 UTC 13 March exhibit the scattered and inaccurate distributions of precipitation when the well-organized intense precipitation occurred (cf. Figs. 6a,b and 5e). This is also true when the condensation processes in these integrations are represented by more sophisticated physical parameterization schemes [e.g., the Fritsch–Chappell (1980) scheme coupled with an explicit moisture scheme (Zhang 1989)]. On the other hand, the model predicts reasonably well the distribution of precipitation associated with the prefrontal squall line and warm front (cf. Figs. 6c and 5e), when the model is initialized at 0000 UTC 13 March. This may be due to the use of better-defined moisture fields in the initial conditions, since QPFs

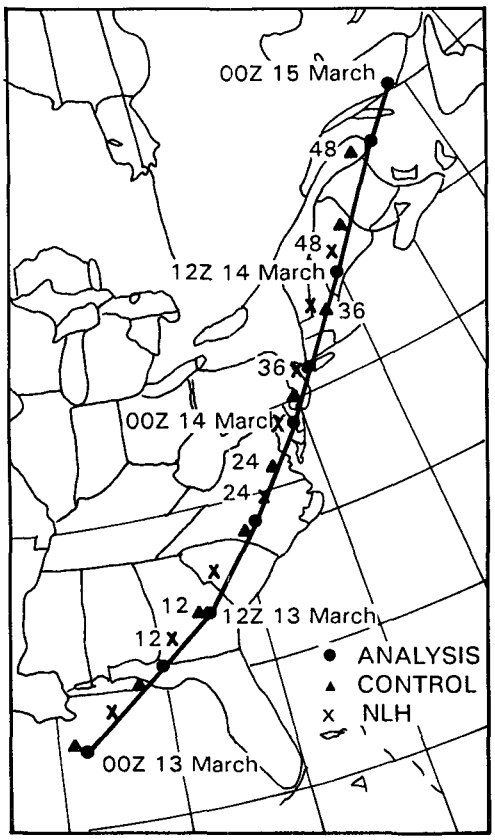

FIG. 7. Analyzed and predicted tracks of the cyclone center during the 48-h period from 0000 UTC 13 March to 0000 UTC 15 March 1993.

are to a certain degree determined by the initial distribution of moisture content once the large-scale forcing is well represented.

We also have found that the same scenario occurs with operational forecasts of the superstorm produced by NMC's Nested Grid Model (NGM) and Regional Spectral Model (e.g., see Juang and Kanamitsu 1994). Therefore, based on the relatively low sensitivity of the predicted storm track and position to the initial conditions, we may conclude that the present storm was driven primarily by certain important large-scale processes that were present in the middle or upper troposphere and were adequately captured by the conventional network during the period of the storm development. By comparison, important details of QPFs are more related to the mesoscale circulations developed within the storm. In view of the above model performance and the evolution of the storm, we shall use the integration that is initialized at 0000 UTC 13 March, as a control prediction to investigate the possible mechanisms by which the storm rapidly intensified. Before doing so, let us examine further how well this integration reproduces other aspects of the superstorm, particularly in the context of QPFs.

5. Control prediction

Since all the model integrations that are initialized at different times can reproduce well the evolution of large-scale flow, we verify only briefly in this section the intensity, path, and upper-level disturbances generated from the 48-h control prediction for the sake of later discussion. We focus more on QPFs because precipitation is an important end product of a model forecast, particularly for the present superstorm in which record-breaking precipitation occurred.

a. Storm intensity and path

Figures 7 and 8 compare the predicted and analyzed MSLPs and tracks of the storm from 0000 UTC 13 to 0000 UTC 15 March 1993. It is evident that the storm track is very well predicted 48 h in advance over a distance of 4000 km. Although the predicted center lags systematically behind the observed, the errors in position are relatively small, particularly during the first 36-h integration. These errors in the path and position are attributable to the use of imperfect initial conditions, since they become smaller when the model is initialized at later times.

The RFE model also predicts reasonably well the intensity of the superstorm, particularly in the first 24 h into the integration. The predicted storm deepens slowly in the first 6 h and then explosively for 18 h, resulting in a 32-hPa drop in MSLP compared to the observed 30-hPa drop. The model appears to overpredict the intensity of the storm after 18 h into the integration; but it does predict well the timing of the filling stage, which started around 0600 UTC 14 March.

b. Large-scale flow

Figure 9 presents horizontal maps for 850-, 500-, and 250-hPa from the 24-h forecast, valid at 0000 UTC 14

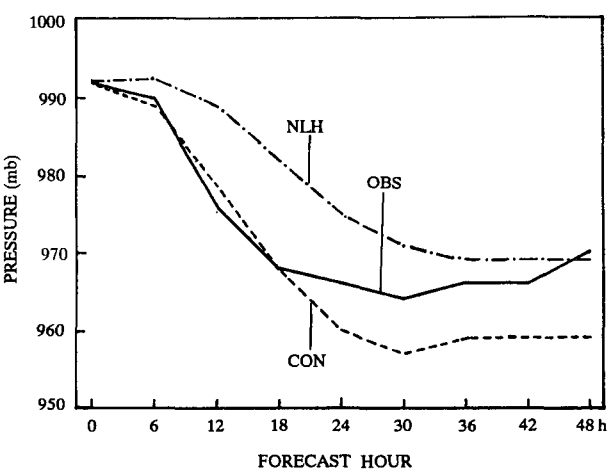

FIG. 8. Time traces of central MSLP (hPa) for the analyzed (OBS), control prediction (CON), and no-latent-heat run (NLH).

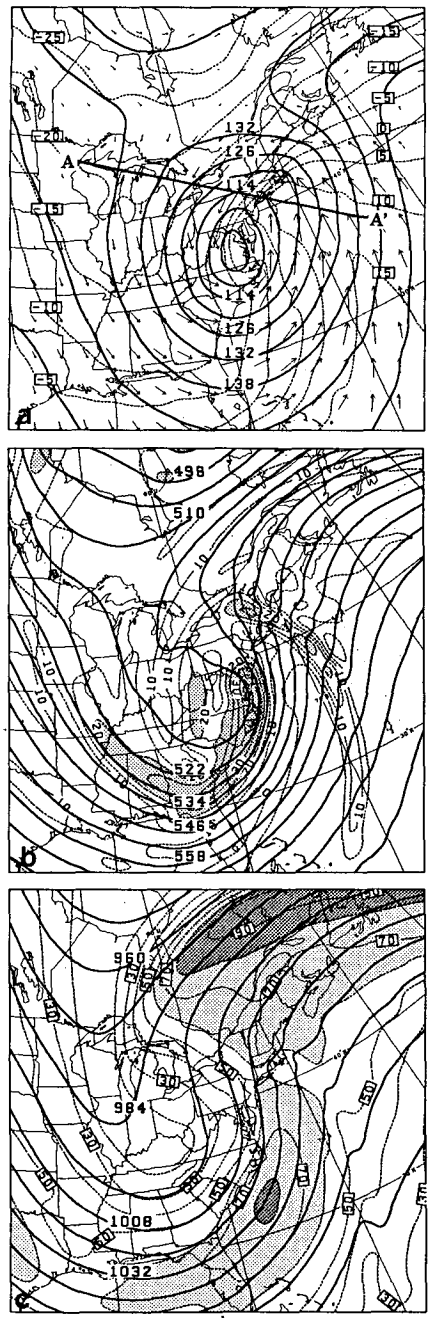

FIG. 9. The 24-h forecast maps valid at 0000 UTC 14 March 1993. (a) The 850-hPa geopotential height (solid) at intervals of 6 dam and temperature (dashed) at intervals of 5°C, superposed with wind vectors. Line AA' in (a) shows the location of the cross section used in Fig. 13. (b) The 500-hPa geopotential height (solid) at intervals of 6 dam and absolute vorticity (dashed) at intervals of 5×10^{-5} s^{-1}. Shading denotes absolute vorticity larger than 20×10^{-5} s^{-1}. (c) The 250-hPa geopotential height (solid) at intervals of 12 dam and isotachs (dashed) at intervals of 10 m s^{-1}. Shadings denote the central portion of jet streaks.

March. The basic height, temperature, and wind fields are all in remarkable agreement with those analyzed (cf. Figs. 9 and 4). At 850 hPa (Fig. 9a), both the strong low-level southerly jet in the warm sector and the packed isotherms from southern New England to southwest Pennsylvania are well reproduced. Deep convection perturbs markedly the middle-level vorticity field ahead of the trough (Fig. 9b); it produces a band of large absolute vorticity ahead of the surface cyclone and along the cold front, indicating that deep convection associated with the prefrontal squall line and cold front assist the surface cyclogenesis to a certain degree. By comparison, this band of vorticity is much weaker in a no-latent-heat run (see section 6a). The intensity and distribution of midlevel baroclinic wave and absolute vorticity (Fig. 9b) and upper-level jet streaks (Fig. 9c) are also well predicted.

c. *Precipitation*

For the purpose of this study, it is important to ascertain whether or not the model could reasonably handle QPFs associated with the superstorm. Figure 10 shows the predicted hourly convective and grid-scale precipitation rates from the 12-h forecast, valid at 1200 UTC 13 March. These maps can be compared to the radar echo analysis (Fig. 5e) that measures the reflectivity of precipitation particles. It is apparent from Fig. 10 that the model captures very well the distribution and orientation of the prefrontal squall line, in which convective precipitation dominates. The predicted convective rainfall band is supported by the strong radar reflectivity (about 46–50 dBZ), high cloud top (14 km), and lightning activity to the east of Florida. In contrast, nearly all of the precipitation elsewhere occurs at the grid scale (cf. Figs. 6c and 10b), which indicates the development of widespread grid-box saturation, particularly in the cold sector and along the warm front. Note the light-precipitation and no-cloud strips in eastern Georgia and northeastern Florida that are in agreement with satellite imagery (cf. Figs. 10 and 5b).

Owing to the use of the regional data assimilation system, the model predicts well the distribution and magnitude of the precipitation during the first 6-h period (cf. Figs. 11a and 11e), including the band associated with the warm front and a heavy precipitation center over southern Georgia and western Florida. Although surface precipitation reports over the oceans are not available, the predicted precipitation patterns conform to satellite observations. However, some discrepancies exist over the Florida peninsula, where the prefrontal squall line was observed to drop a larger amount of convective precipitation than that predicted.

Six hours later, the predicted precipitation amount increases in magnitude as the system moves northeastward and intensifies. There are two precipitation centers, one in the stratiform region over northwestern Georgia and the other associated with the prefrontal

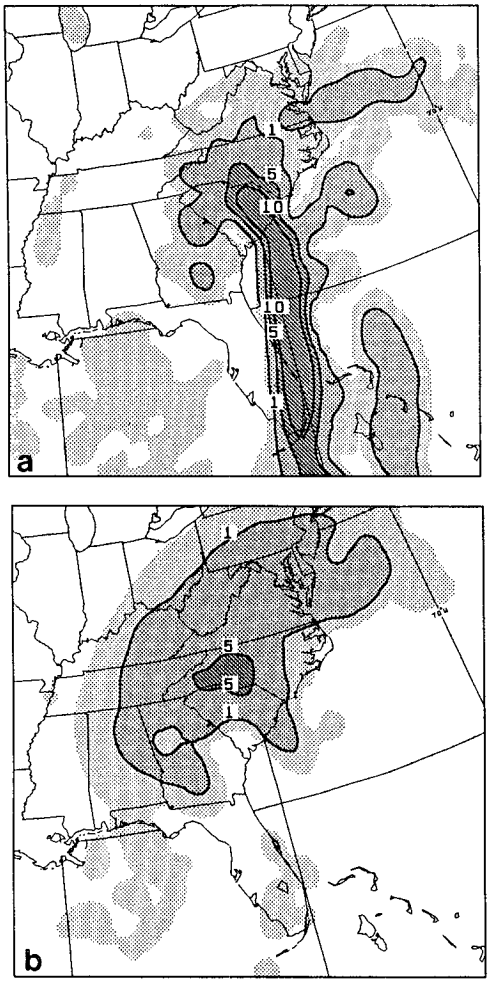

FIG. 10. Distribution of the hourly (a) convective and (b) grid-scale precipitation rates (mm h^{-1}) from 12-h prediction, valid at 1200 UTC 13 March 1993.

squall line over Florida. In general, the model appears to overpredict the localized central portion of stratiform precipitation and underpredict the maximum convective precipitation. Nonetheless, the general pattern, orientation, and location of precipitation agree well with the observed (cf. Figs. 11b and 11f). For example, the model reproduces the heavy stratiform precipitation strip that is oriented roughly parallel to the Appalachians.

For the 6-h periods ending at 1800 UTC 13 March and 0000 UTC 14 March, the predicted precipitation patterns over land are in good agreement with the observed (cf. Figs. 11c,d and Figs. 11g,h). Since the squall line had dissipated during this period except close to the cyclone center, most of the precipitation was generated in the stratiform region. The model reproduces well the heavy precipitation that occurred to the northeast of the cyclone center. Maximum precipitation exceeds 40 mm in 6 h. The results suggest that the model physics and initial conditions used for the study are sufficiently realistic so that the model results can be used to investigate the processes leading to the rapid intensification of the superstorm.

d. Vertical wind structure

As a further indication of the model's performance, Fig. 12 compares the predicted time series of wind profiles to those obtained by McGill University's wind profiler (Rogers et al. 1993). Note that Montreal is located in the cold sector throughout the cyclone life cycle, experiencing the approach of the cyclone from the southwest. The model reproduces a northeasterly low-level jet that intensifies as the system approaches and weakens as the cyclone fills and moves away. The intensity of the jet exceeds 30 m s^{-1}. Above the low-level jet, the model produces a rapid veering of the winds in the 800–600-hPa layer, indicating the presence of strong warm advection. Higher up, both the observed and predicted wind profiles capture a portion of the upper-level jet streak. The predicted timing, vertical distribution, and magnitude of these large-scale elements are all in good agreement with the high-resolution wind profiler measurements.

6. Possible deepening mechanisms

After documenting that the control prediction reproduces well the basic large-scale and mesoscale events associated with the superstorm, it is possible to use this prediction to investigate various processes and structural entities that are associated with the rapid deepening of the storm. In this section, we examine the effects of latent heat release, prestorm environmental conditions, jet streak–induced circulations, and tropopause depression on the deepening of the cyclone. Of course, baroclinic instability is always the basic mechanism responsible for cyclogenesis.

a. Effect of latent heat release

Since the superstorm dropped a tremendous amount of precipitation, latent heat release may have played an important role in the deepening of the cyclone. Thus, a sensitivity experiment is conducted, in which all the model parameters are kept identical to those of control prediction (experiment CON) except that the latent heat release associated with the grid-scale and subgrid-scale precipitation is turned off (experiment NLH). Then, all differences between the two runs can be attributed to the development of condensation processes.

It is evident from Fig. 7 that in the absence of latent heating, the path of the storm is very similar to that in CON. This further indicates that large-scale dry dynamics (or baroclinicity) controls the movement of the storm. However, the NLH storm is considerably weaker in intensity and slower in displacement than the CON storm (see Figs. 7 and 8). The effect of latent

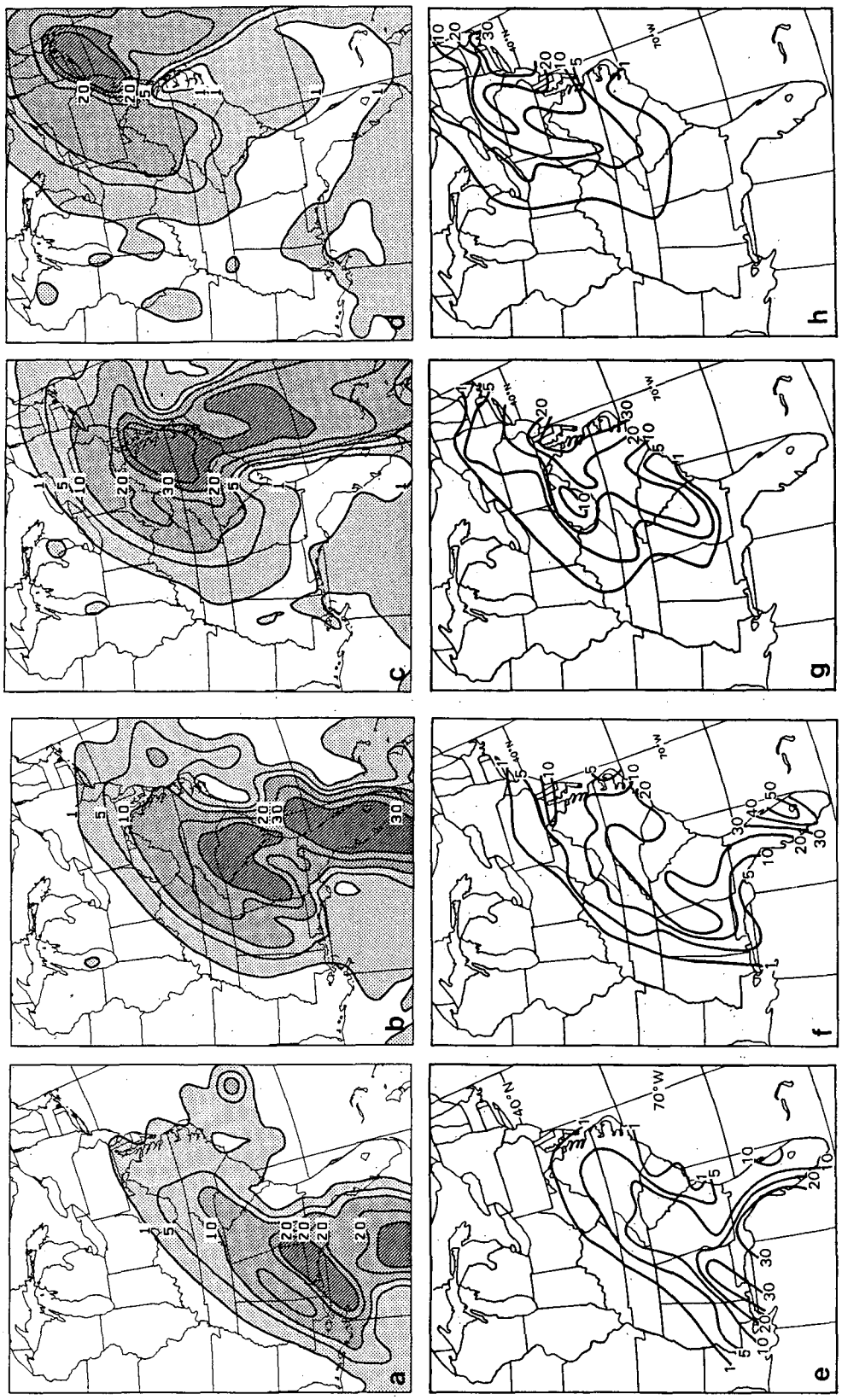

FIG. 11. Distribution of 6-h accumulated precipitation prediction (mm) ending at (a) 6-h, (b) 12-h, (c) 18-h, and (d) 24-h integration, which are valid at (e) 0600 UTC, (f) 1200 UTC, (g) 1800 UTC 13 March, and (h) 0000 UTC 14 March 1993, respectively. Panels (e)–(h) are drawn according to operational observations.

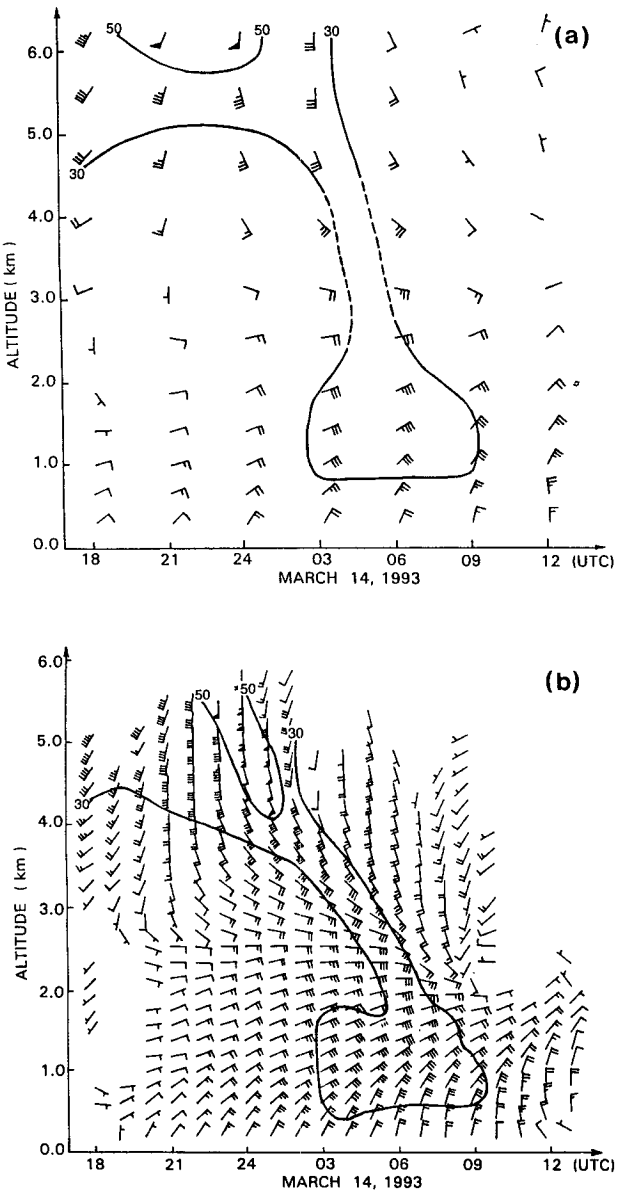

FIG. 12. Time–height cross section of horizontal winds and isotachs (m s^{-1}) at Montreal from (a) model prediction and (b) wind profiler measurements. A full bar is 10 m s^{-1}, a half bar 5 m s^{-1}, and a flag 50 m s^{-1}. The 30 and 50 m s^{-1} isotachs are also shown.

heating appears to be particularly significant during the first 12-h integration, in which the latent heating accounts for the explosive deepening of the storm (i.e., an 11-hPa MSLP drop in 6 h). This period coincides with the rapid development of the prefrontal squall line and extensive stratiform precipitation along the warm front. Without the latent heating, the NLH storm deepens only 2–3 hPa during the first 6 h, but then it deepens at a rate of 14 hPa in 12 h as compared to a 19-hPa MSLP drop in the CON run. These comparable deepening rates imply a reduced impact of latent heating and an increased influence of other processes on the storm's development after 12 h into the integration. Nevertheless, latent heating accounts for about 40% of the total deepening by the end of the 36-h integration.

While the above results are not surprising, given the findings of previous investigations, it is important to understand the ways in which moist processes contribute to the storm's development. Figure 13 presents a vertical cross section of the predicted 24-h temperature and height differences between experiments CON and NLH. In general, the moist processes tend to produce net warming in the layer above the trough axis of the height difference with a maximum value of greater than 12°C occurring near 350 hPa and net cooling below with a minimum value of less than −6°C occurring at 850 hPa. Hydrostatically speaking, this profile of net warming (including diabatic and adiabatic heating and temperature advection) will increase the upper-level and decrease the lower-level height of isobaric surfaces, as shown in Fig. 13. Of importance is that although the intense net warming occurs in the upper troposphere, the most significant dynamic response appears in the lower troposphere, with the maximum height falls occurring near the surface. According to Hirschberg and Fritsch (1991), a given temperature anomaly in a layer of air high in the atmosphere would produce a larger height perturbation near the surface than an equal temperature anomaly in a layer of air low in the atmosphere. The low (upper)-level height falls (rises) tend to increase mass and moisture convergence (divergence) in the lower (upper) troposphere, thereby enhancing the vertical ageostrophic circulations associated with the cyclogenesis. On the other hand, the horizontal heating structure produces stronger height gradients in the lower half of the troposphere that help accelerate the storm's movement. Moreover, warming the air in the warm sector and cooling the air in the cold sector enhances the large-scale baroclinicity in a deep layer (up to 300 hPa), most significantly around the trough axis of differenced heights. Evidently, these vertical and horizontal net heating structures are both favorable for the production of additional available potential energy and the increased conversion to kinetic energy for rapid cyclogenesis.

b. Effect of the prestorm environment

The generation of the tremendous amount of precipitation in the superstorm also indicates the presence of favorable thermodynamic conditions in the prestorm environment. In particular, since most of the precipitation occurs along the prefrontal squall line and over the stratiform region along the warm front, potential and slantwise instabilities may be the mechanisms by which latent heat release plays an important role in the explosive deepening of the storm. For this purpose, the modified lifted index (MLI, Fig. 14), obtained by subtracting equivalent potential temperature θ_e near the

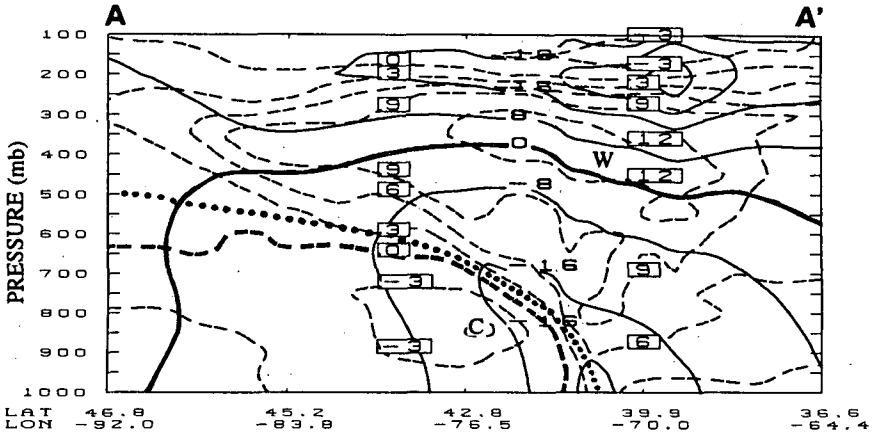

FIG. 13. Vertical cross section of the height differences (solid) at intervals of 8 m and the temperature differences (dashed) at intervals of 3°C between experiments CON (control) and NLH (no latent heating)—that is, CON minus NLH, from 24-h integration, which is valid at 0000 UTC 14 March 1993. Dotted line indicates the trough axis of the height differences. The cross section is taken along line *AA'* given in Fig. 9a.

surface from saturated θ_e at 500 hPa, is utilized to estimate the potential for deep upright convection (see Reed et al. 1993), while vertical cross sections of absolute momentum ($M = v + fx$) and θ_e (Fig. 15) are employed to examine the role of slantwise instability (see Bennetts and Hoskins 1979; Emanuel 1983a,b).

It is apparent from Fig. 14 that negative (positive) values of MLI are distributed in the warm (cold) sector, with the zero isopleth roughly corresponding to the surface warm and cold fronts. Thus, potentially unstable (stable) conditions dominate in the warm (cold) sector. The rapid development of the intense prefrontal squall line at this stage (e.g., 1200 UTC 13 March) is also an indication of the potentially unstable environment that has developed prior to this time. This instability is mainly released in a narrow region of intense ascending motion associated with the squall line and then suppressed by the passage of the cold front (Figs. 14 and 15a). Nevertheless, a deep layer of potential instability still exists immediately behind the cold front due to the existence of subsiding air. Further behind, a shallow layer of potential instability is obvious and is probably produced by strong heat and moisture fluxes from the underlying warm ocean, where widespread low-level cumulus clouds or streamers were observed (see Fig. 5). The development of the deep unstable layer in the warm sector suggests the importance of the advection of tropical maritime air ahead of the surface cyclone and the cumulative effects of sensible and latent heat fluxes from the oceans. In particular, when these two processes (the advection of tropical marine air ahead of the cyclone, and the cumulative effects of latent and sensible heating from the ocean) are coupled with the development of the low-level jet in the warm sector, a significant amount of moisture can be transported into the squall and frontal regions for latent heat release during the explosively deepening stage. In this respect, Hedley and Yau (1991) showed an example of numerical simulation with idealized initial conditions on how an imposed SST anomaly can generate a potentially unstable environment in the warm sector.

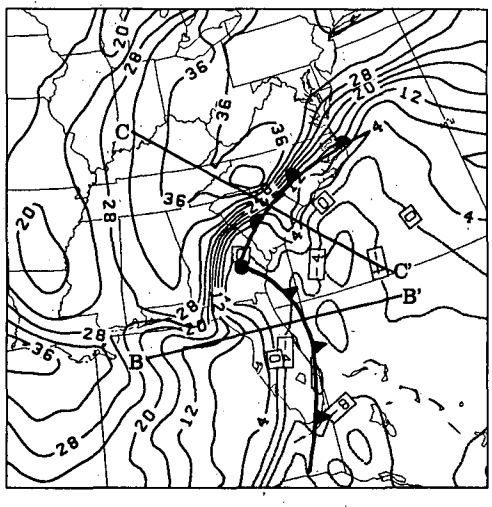

FIG. 14. Modified lifted index at intervals of 4 K from 12-h integration, valid at 1200 UTC 13 March 1993. Distribution of the surface warm and cold fronts is superposed and the location of the cyclone center is given by a solid circle. Lines *BB'* and *CC'* denote the locations of the cross sections used in Fig. 15.

While upright convection associated with the squall line dominates the release of potential instability along the cold front, slantwise convection appears to be the process leading to the release of the instability along the warm front. Specifically, Fig. 15b shows the presence of little or no upward motion in the warm sector and strong sloping ascent along the well-defined warm

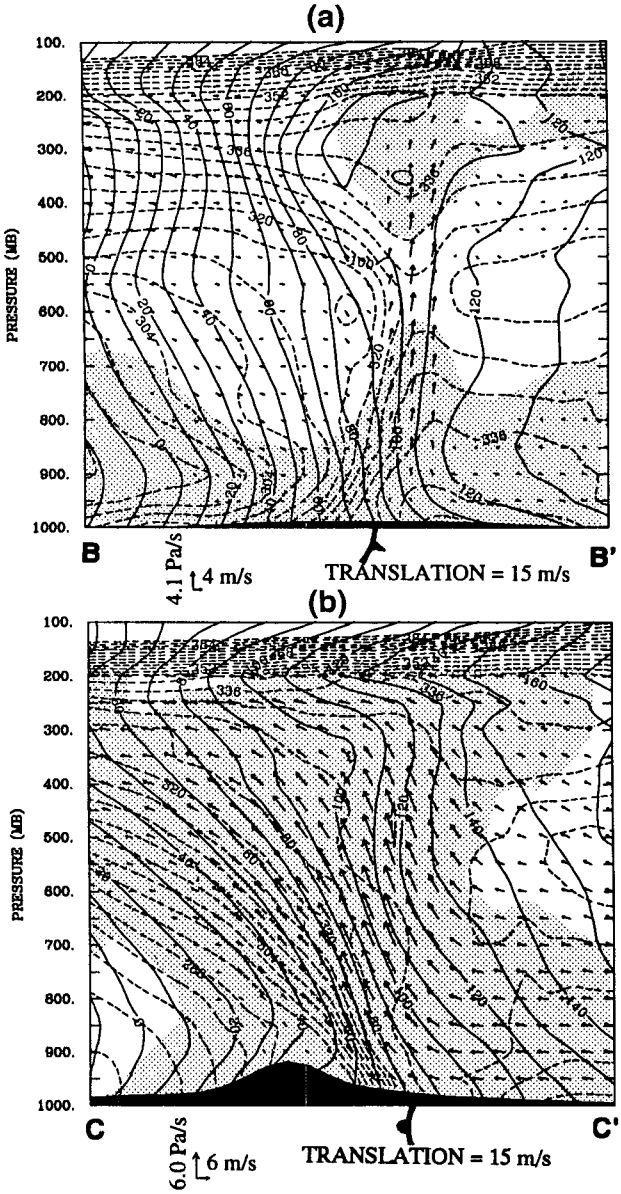

FIG. 15. Vertical cross sections of absolute momentum (solid) at intervals of 10 m s^{-1} and equivalent potential temperature (dashed) at intervals of 4 K, superposed with along-plane flow vectors from 12-h integration valid at 1200 UTC 13 March 1993 along (a) line *BB'* and (b) line *CC'* given in Fig. 14. Shading denotes the distribution of cloudiness, as determined by relative humidity (RH) larger than 80%. The positions of cold and warm fronts are indicated on the abscissa.

front where the flow vectors lie almost "parallel" to the θ_e surfaces. This suggests that the potentially unstable air is being transported in the southerly flow into the warm frontal zone, where lifting to saturation occurs and the instability is released. Since the sloping ascent region is saturated (see the shaded area), the vertical configuration of M and θ_e surfaces implies the presence of moist symmetric instability in the sloping flow, as has also been noted by Kuo and Reed (1988), Reuter and Yau (1990), and others. The characteristic of slantwise neutrality in the frontal zone is in agreement with the observational results of Emanuel (1988) and Reuter and Yau (1990).

c. *Possible effect of jet streak–induced circulations*

Numerous observational studies have shown the importance of transverse ageostrophic circulations associated with upper-level jet streaks in rapid cyclogenesis (e.g., Uccellini and Johnson 1979; Uccellini et al. 1984; Uccellini et al. 1987). However, in other cases such transverse ageostrophic circulations could not be found (e.g., Colman et al. 1994). Since the storm in the present case was situated in the right entrance region of an upper-level jet streak all the time, we examine whether or not the jet streak–induced circulations would be essential in determining the intensification of the storm.

Figure 16a shows the distribution of vertical ageostrophic circulations from the 12-h forecast of the NLH run, which is taken slightly ahead of the surface cyclone along a line normal to the 250-hPa jet streak. It is obvious that a thermally direct transverse ageostrophic circulation is present in the entrance region of the upper-level jet streak, even in the absence of latent heating. A similar but weaker transverse circulation is also present in the entrance region in the model initial conditions (not shown). This dynamically induced ageostrophic circulation is a result of the forcing from both the jet streak and the warm front that are more pronounced at upper and lower levels, respectively. The line of θ_e = 285 K separates roughly the upward from downward branches of the transverse circulation, with strong convergence occurring in the lowest 100-hPa layer and divergence at the jet streak level. Within the entrance region, the southeasterly warm and moist air ascends from the boundary layer in the warm sector into the upper-level jet streak, while the cold and dry air descends underneath the warm front surface. To our knowledge, there is presently no effective method available for isolating the individual circulations associated with the jet streak and the warm front. We will, therefore, discuss the circulation associated with the jet streak and that associated with the front together as a whole. It should be noted that the transverse circulations associated with the jet streaks and fronts can be diagnosed in the quasigeostrophic framework owing to the presence of strong baroclinicity. Their importance in cyclogenesis can be seen only when they are coupled with latent heat release. In particular, these transverse circulations appear to play a role in helping transport potentially unstable air in the warm sector into the warm-frontal zone and then release the moist symmetric instability.

When the latent heat release is allowed during the integration (i.e., the CON run), the upward motion

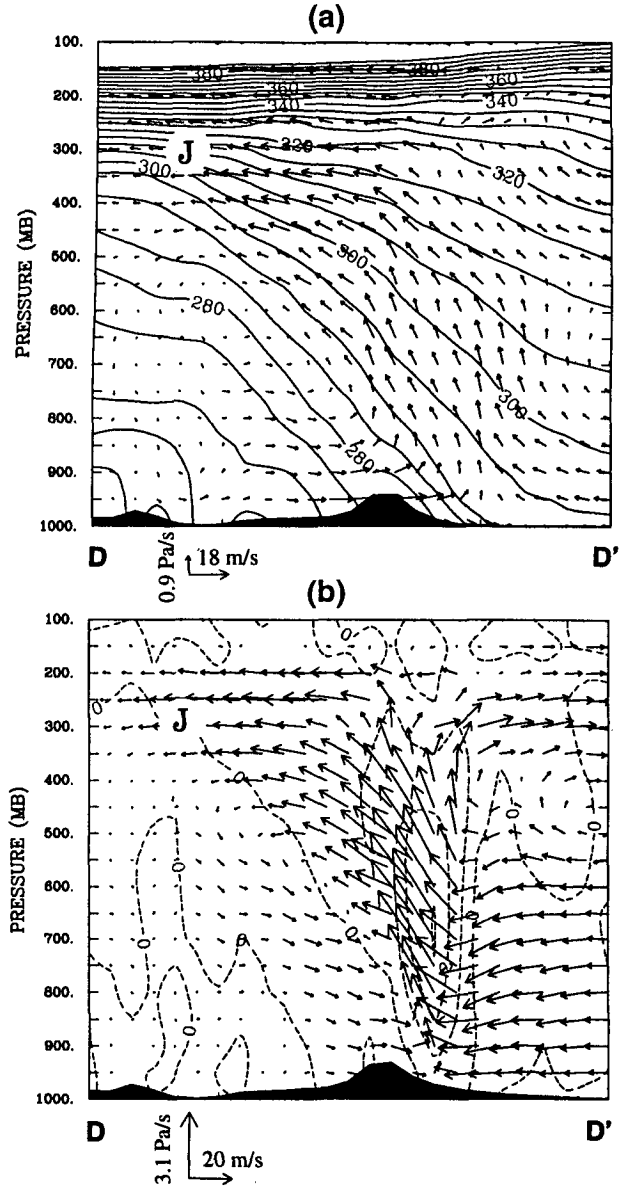

FIG. 16. Vertical cross sections of ageostrophic circulations for (a) experiment NLH (no latent heating) and (b) the difference field between experiments CON and NLH from 12-h integration, valid at 1200 UTC 13 March 1993. Solid lines are isentropes at intervals of 5 K and dashed lines vertical motion ω at intervals of 1.0 Pa s^{-1}. The cross section is taken along line DD' given in Fig. 3a.

branch of the transverse circulation is substantially enhanced, as can be seen from the difference field given in Fig. 16b. The ascending zone is also significantly narrowed and concentrated closer to the warm frontal zone. Specifically, the net upward motion due to latent heating more than triples that induced by the jet streak and warm front (cf. Figs. 16a and 16b). The low-level southerly jet intensifies significantly; the net increase due to latent heating more than doubles that induced by dry dynamics. The enhanced ascending branch implies the development of stronger influx of high θ_e air overrunning the frontal surface that is favorable for the establishment of a positive feedback among latent heat release, low (upper)-level convergence (divergence) and surface-pressure fall. This in turn helps intensify the low-level jet and strengthen the vertical ageostrophic circulation and the coupling of the low-level flow with upper-level disturbances. However, the inclusion of latent heating does not enhance much the descending branch of the circulation, since it is mostly driven by larger-scale baroclinic processes.

The above results indicate that the ageostrophic circulation may have played a role in establishing a dynamic link in the vertical by inducing a southerly flow component at the lower levels and by enhancing the warm frontal lifting of the maritime boundary layer air leading to latent heat release. Clearly, this process is important during the cyclone's incipient stage. Once the latent heating becomes dominant (i.e., during the rapidly deepening stage), the jet-induced circulation component can provide only a favorable environment within which warm and moist air is transported into the warm-frontal zone. In other words, the jet streak–induced circulation does not seem to be crucial in determining the final intensity of the superstorm. In particular, the surface cyclone was slowly filling after 0000 UTC 14 March when the storm was located at the right entrance region of the jet A and the left exit region of the jet B (see Fig. 4) within which the jet streak–induced circulation was supposedly more favorable for cyclogenesis according to Uccellini and Kocin (1987).

d. Effect of tropopause depression

As mentioned previously, the superstorm deepened in an area of positive vorticity advection associated with two intensifying short-wave troughs aloft. Hence, we use the dynamic variable, potential vorticity (PV), to qualitatively investigate the likely interaction of the surface development with the upper-level disturbances. Potential vorticity, in the form introduced by Ertel (1942), is given by

$$\mathrm{PV} = \frac{1}{\rho}\left[\frac{\partial\theta}{\partial x}\left(\frac{\partial w}{\partial y}-\frac{\partial v}{\partial z}\right)+\frac{\partial\theta}{\partial y}\left(\frac{\partial u}{\partial z}-\frac{\partial w}{\partial x}\right)+\frac{\partial\theta}{\partial z}\left(\frac{\partial v}{\partial x}-\frac{\partial u}{\partial y}+f\right)\right], \quad (1)$$

where u, v, and w are wind speeds (m s^{-1}) in the x, y, and z directions, respectively; θ is potential temperature; f is the Coriolis parameter; and ρ is the density of air. Potential vorticity is conserved in the absence of diabatic and frictional effects. Although PV given in Eq. (1) is three-dimensional, it is mostly determined by the third term in the parenthesis—that is, the product of static stability and vertical absolute vorticity.

Hoskins et al. (1985) provided an exhaustive review of the use of PV and showed that rapid cyclogenesis can occur when a region of PV anomaly associated with a tropopause depression overruns a low-level baroclinic zone. Moreover, Hoskins et al., following Bretherton (1966), demonstrated that a surface temperature anomaly can be regarded as equivalent to a concentrated PV anomaly contained in a thin surface layer, with locally warm air associated with cyclonic vorticity and cold anomaly related to anticyclonic vorticity. From the discussion in section 2, it is seen that a surface warm anomaly exists over the Gulf of Mexico at the early stage of the storm development (Fig. 1a), and later on a strong warm (cold) anomaly is created in the warm (cold) sector by strong warm (cold) advection (Figs. 2b–4b). These temperature anomalies may also have some effects on the storm development. In the present paper, we present only some results to examine qualitatively the possible effects of the tropopause depression PV on the storm development.

Figures 17a–c present the distribution of predicted PV at 400 hPa (solid), superposed with PV at 850 hPa (dashed), valid at 0000, 1200 UTC 13, and 0000 UTC 14 March, respectively. Ground-relative flow vectors and cloud distribution at 400 hPa are also superposed. At 0000 UTC 13 March (Fig. 17a), there are two distinct features of PV at 400 hPa: a tongue of large PV (>3 PVU, 1 PVU = 10^{-6} m^2 K s^{-1} kg^{-1}) in the central United States and another PV anomaly over the western Gulf of Mexico. The northern PV tongue is distributed in the same zone as the midlevel northwestern trough, while the southern PV anomaly coincides with the midlevel southeastern trough (cf. Figs. 17a and 2c). If a typical value of 1.5 PVU is used to define the "dynamic" tropopause, such an extensive area of PV anomaly is indicative of a tropopause depression, a process of dry intrusion of stratospheric air. This dry stratospheric intrusion can be further evidenced by the model-predicted cloud field, which shows a cloud-free region associated with the PV tongue (drying implies descending) and nearly saturated conditions to its east (saturation implies ascending). Thus, the intensification of the two midlevel troughs is a consequence of continued descent of the stratospheric dry and warm air. It should be mentioned that the two PV anomalies are completely separated below 400 hPa. Unlike the Presidents' Day cyclone in which the surface cyclogenesis and tropopause depression developed separately during the incipient stage (Uccellini et al. 1985; Uccellini 1986; and Whitaker et al. 1988), the tropopause depression in the present case appears to intensify concurrently with the surface cyclogenesis. In particular, the flow vectors in the vicinity of the storm suggest that the PV in the southern depression tip is being advected toward the cyclone center by southwesterly currents. This advection of high PV would increase the cyclonic vorticity associated with the storm (Hoskins et al. 1985). Since this PV anomaly

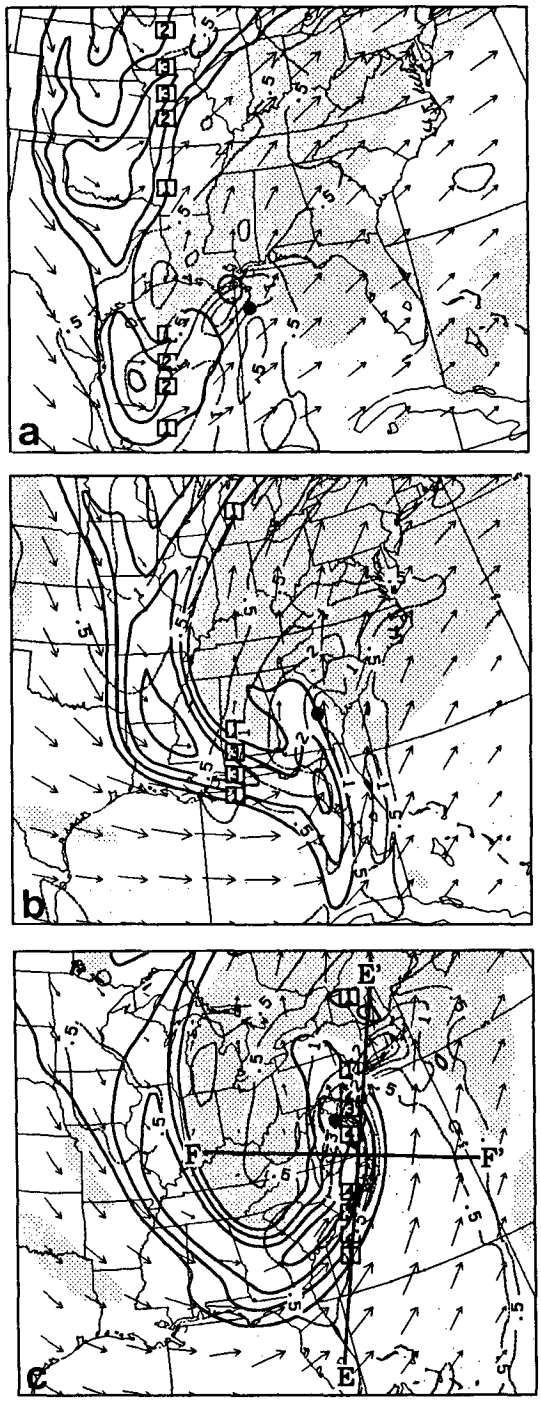

FIG. 17. Distribution of 400-hPa (solid) and 850-hPa (dashed) potential vorticity (PVU) superposed with 400-hPa wind vectors from (a) 0-h, (b) 12-h, and (c) 24-h integrations, valid at 0000 and 1200 UTC 13 March, and 0000 UTC 14 March 1993. Shadings denote the distribution of cloudiness that is determined by relative humidity larger than 80%. The location of the cyclone center is given by a solid circle. Lines *EE'* and *FF'* denote the locations of the cross sections used in Fig. 19.

penetrates downward well below 400 hPa, the tropopause depression appears to have a decisive role in the rapid spinup of the cyclone during this stage. At 850 hPa, an elongated zone of PV is distributed downstream of the upper-level PV anomaly along the prefrontal squall line, with a maximum value exceeding 2 PVU located to the northwest of the cyclone center. Most of this low-level concentration of PV is attributable to the latent heat release in convective and stratiform clouds (Davis et al. 1993). Note that both the lower- and upper-level PV anomalies are in a favorable phase for cyclonic development.

By 1200 UTC 13 March, the southern PV anomaly has been advected to the western Florida peninsula (Fig. 17b). Strong advection of PV toward the cyclone center occurs during this explosively deepening stage. The dry stratospheric intrusion is evident over the Florida peninsula and Georgia as represented by the low relative humidity at 400 hPa. Meanwhile, the PV anomaly to the west is being advected eastward into the base of the short-wave trough, with its magnitude increased over 4 PVU; however, its effect may have not been felt entirely by the surface cyclone at this time. The lower-level PV has intensified further and become better organized. High PV has also expanded into a larger area near the cyclone center. Six hours later, the two upper-level PV centers merge completely, as do the two mid-level short-wave troughs, but still with a favorable phase with the surface cyclone (not shown).

By 0000 UTC 14 March, the upper-level PV ribbon has wrapped around the short-wave trough (Fig. 17c). The surface cyclone is being overtaken by the leading portion of the PV ribbon; but it is still in an area affected by positive PV advection. This explains why the surface cyclone enters gradually the occlusion stage (Fig. 4) but it still continues to deepen (Fig. 8). Nevertheless, this marks the end of the storm's explosively deepening stage.

When the latent heating is turned off (i.e., in experiment NLH), the vertical PV structure as well as its influence on the cyclogenesis differs from that in experiment CON. In particular, the slow movement of the storm in the absence of latent heating places the cyclone under a much less favorable condition (Fig. 18a). Specifically, the southern PV anomaly is quickly advected eastward with merely a brief period of overlap with the cyclone; the PV advection is even not directed toward the cyclone center (Fig. 18a). Hence, the NLH cyclone experiences slight deepening during the first 12-h period, as shown in Fig. 8. Only when the PV tongue to the west wraps around the short-wave trough, can strong PV advection into the cyclone center take place (Fig. 18b). This process occurs after 12 h into the integration, corresponding to a 14-hPa deepening in 12 h, a rate comparable to that which occurred in CON (Fig. 8). Therefore, the latent heating appears to be instrumental in coupling the surface development with the upper-level PV anomalies. In the present case,

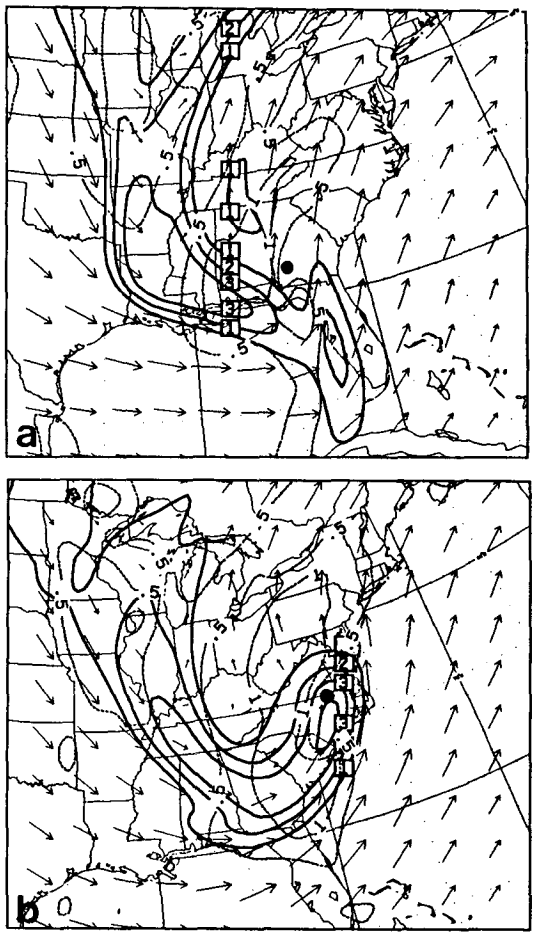

FIG. 18. As in Fig. 17 but from (a) 12-h, and (b) 24-h integrations for experiment NLH (no latent heating), valid at 1200 UTC 13 March and 0000 UTC 14 March 1993, respectively.

the latent heat release helps generate and maintain a favorable upstream tilt of PV during the first 12-h integration such that the advection of stratospheric PV toward the cyclone center can be optimized.

To further examine the vertical structure of the PV features at the mature stage of the cyclone, Fig. 19 presents two vertical cross sections of PV taken near the cyclone center along lines parallel and normal to upper-level flow vectors. Within the framework of PV thinking, we can also infer to some degree the interactions between the various PV features based on their relative positions. There are two distinctive PV concentrations in the vertical: one center located at 300 hPa in the cloudless dry air and another center in the 900–800-hPa layer within the cloudy air. Descending motion prevails within the upper-level PV region except to its northern edge where upward motion occurs as a result of latent heat release along the warm front. If the isopleth of 80% relative humidity, approximately following 1-PVU contour, is utilized to separate the air mass of these two different origins, the upper-level PV con-

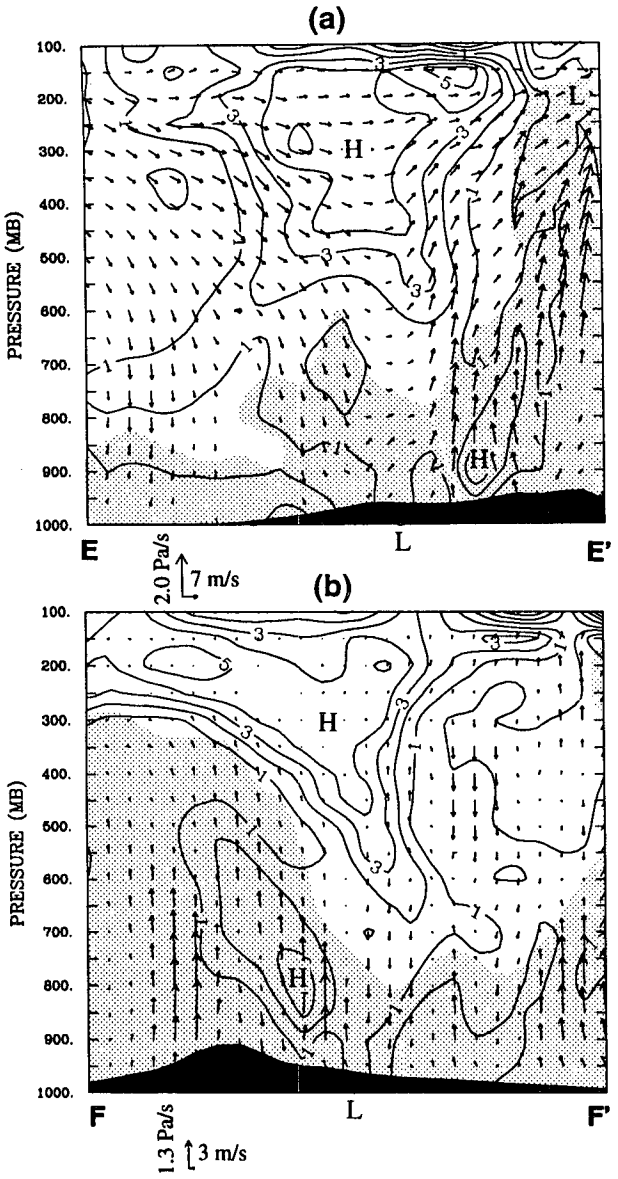

FIG. 19. Vertical cross sections of potential vorticity (PVU, solid) superposed with along-plane flow vectors, along (a) line *EE'*, and (b) line *FF'* in Fig. 17c from 24-h integration, valid at 0000 UTC 14 March 1993. Shadings denote the vertical distribution of cloudiness determined by relative humidity larger than 80%.

centration is much more distinct than its low-level counterpart. We can see that the dry stratospheric high-PV air reaches down to 700 hPa near the cyclone center, with another strip of high PV around it. The later PV is concentrated in a relatively small volume and is produced mainly by latent heating. Meanwhile, a PV minimum is also created aloft. This result is consistent with the theory of Hoskins et al. (1985) that diabatic heating tends to create PV below and destroy it above, acting to "propagate" PV downward. The descending tropopause high-PV air above the surface low implies that the cyclonic circulation induced by the PV anomaly may have helped the surface cyclone development. To quantitatively assess its importance and its interactions with the low-level PV features, a piecewise PV inversion as proposed by Davis and Emanuel (1991) is necessary. This task is planned for the future.

7. Summary and conclusions

In this study, the evolution of "the storm of the century" that occurred in March 1993 is documented using conventional observations, and the model predictability and possible deepening mechanisms of the storm are investigated using a newly implemented mesoscale version of the operational Canadian Regional Finite-Element (RFE) Model with a grid size of 50 km. Observational analysis reveals that the storm began as a low-level weak vortex in northern Mexico and developed rapidly through condensation processes as it moved over the anomalously warm Gulf of Mexico. Then, the storm deepened explosively as two midlevel shortwave troughs approached, merged, and interacted with the surface cyclone.

Several sensitivity experiments are performed by initializing the model at different synoptic times in order to examine the model predictability of the superstorm. It is found that while the RFE model can predict well the large-scale background flow associated with the storm days in advance, it fails to predict various important mesoscale elements when it is initialized at earlier times with fields that contain weak signals of the low-level circulations. However, when the initial conditions contain reasonably the signals of the storm, the model has a considerable skill in predicting those mesoscale elements, such as a prefrontal squall line, upper- and low-level jets, as well as their associated precipitation. The result underlines the importance of using realistic initial conditions in order to improve quantitative precipitation forecasts and severe weather warnings associated with winter storms.

The role of latent heat release in the cyclogenesis is examined by comparing simulations with and without latent heating. It is found that in the absence of latent heating the predicted cyclone is considerably weaker in intensity and slower in displacement. The latent heating occurs primarily through the release of potential instability in the prefrontal squall line and moist symmetric instability within the warm frontal zone. The development of the low-level jet, coupled with sensible and latent heat fluxes from the oceans, plays an important role in transporting high-θ_e air into the frontal zone for the release of instabilities. The impact of latent heating appears to be particularly significant during the first 18-h integration when explosive deepening occurs; it accounts for roughly 40% of the total deepening. The effects of latent heating are to (i) increase the upper-level and decrease the lower-level height of isobaric

surfaces; (ii) strengthen horizontal height gradients in the lower troposphere; and (iii) enhance the large-scale baroclinicity in a deep layer of the troposphere. Furthermore, the latent heat release appears to help maintain a favorable phase between the surface cyclone and an upper-level PV anomaly such that positive PV advection is optimized. The heating-induced circulation could also provide an important coupling of the cyclogenesis with various low- to upper-level disturbances.

The importance of the upper-level jet streak–induced circulations in the deepening of the storm is also examined. It is found that a thermally direct ageostrophic circulation is present in the entrance region of the upper-level jet streak at all times, even in the absence of latent heating. The jet-induced circulation appears to play a role in establishing a dynamic link in the vertical by inducing a southerly flow component at the lower levels and by enhancing the warm-frontal lifting of the maritime boundary layer air leading to latent heat release. However, it does not seem to be crucial in determining the final intensity of the superstorm.

A PV diagnosis indicates that the intensification and merging of the midlevel troughs occur as a result of the pronounced descent of stratospheric PV-rich air associated with tropopause depressions. The tropopause depression appears to be an important upper-level forcing that determines the rapid deepening as well as the model predictability of the storm, in addition to the basic large-scale baroclinic forcing. We conclude that the tropopause depression, latent heat release, weak static stability, the ageostrophic circulation associated with the jet streak and front, and surface sensible and latent heat fluxes act together to determine the amplification and evolution of "the storm of century," although their relative importance differs at different stages of the storm's development and they do not occur in isolation in the real atmosphere.

Acknowledgments. We thank R. Hogue for helpful consultation on the Regional Data Assimilation System, Prof. R. Rogers for providing Fig. 12b, and Ms. U. Seidenfuss for her expert work in the preparation of some figures. We also thank the two anonymous reviewers for their thorough reviews, and the editor, Frederick Sanders, for his helpful comments, all of which led to significant improvements to the manuscript. This research was supported by "Fonds pour la Formation de chercheurs" (FCAR) of the province of Quebec, and by the Atmospheric Environment Service (AES) of Environment Canada. The first author (Z. Huo) was also supported by a graduate scholarship from FCAR.

REFERENCES

Anthes, R. A., Y.-H. Kuo, and J. R. Gyakum, 1983: Numerical simulations of a case of explosive marine cyclogenesis. *Mon. Wea. Rev.*, **111,** 1174–1188.

Bell, G. D., and L. F. Bosart, 1993: A case study diagnosis of the formation of an upper-level cutoff cyclonic circulation over the eastern United States. *Mon. Wea. Rev.*, **121,** 1635–1655.

Bennetts, D. A., and B. J. Hoskins, 1979: Conditional symmetric instability—A possible explanation for frontal rainbands. *Quart. J. Roy. Meteor. Soc.*, **105,** 945–962.

Benoit, R., J. Côté, and J. Mailhot, 1989: Inclusion of a TKE boundary layer parameterization in the Canadian regional finite-element model. *Mon. Wea. Rev.*, **117,** 1726–1750.

Bosart, L. F., 1981: The Presidents' Day snowstorm of 18–19 February 1979: A subsynoptic-scale event. *Mon. Wea. Rev.*, **109,** 1542–1566.

——, and S. C. Lin, 1984: A diagnostic analysis of the Presidents' Day snowstorm of February 1979. *Mon. Wea. Rev.*, **112,** 2148–2177.

Bretherton, F. P., 1966: Critical layer instability in baroclinic flows. *Quart. J. Roy. Meteor. Soc.*, **92,** 325–334.

Carlson, T. N., 1980: Airflow through midlatitude cyclones and the comma cloud pattern. *Mon. Wea. Rev.*, **108,** 1498–1059.

Chouinard, C., J. Mailhot, H. L. Mitchell, A. Staniforth, and R. Hogue, 1994: The Canadian regional data assimilation system: Operational and research applications. *Mon. Wea. Rev.*, **122,** 1306–1325.

Colman, B. R., E. I. Tollerud, and R. S. Collander, 1994: Assessing the use of upper-level jet streaks for the operational prediction of winter precipitation. Preprints, *Symp. on the Life Cycle of Extratropical Cyclones,* Bergen, Norway, Univ. of Bergen, 274–279.

Davis, C. A., and K. A. Emanuel, 1991: Potential vorticity diagnostics of cyclogenesis. *Mon. Wea. Rev.*, **119,** 1929–1953.

——, M. T. Stoelinga, and Y.-H. Kuo, 1993: The integrated effect of condensation in numerical simulations of extratropical cyclogenesis. *Mon. Wea. Rev.*, **121,** 2309–2330.

Deardorff, J. W., 1978: Efficient prediction of ground surface temperature and moisture with inclusion of a layer of vegetation. *J. Geophys. Res.*, **83,** 1889–1903.

Emanuel, K. A., 1983a: The Lagrangian parcel dynamics of moist symmetric instability. *J. Atmos. Sci.*, **40,** 2368–2376.

——, 1983b: On assessing local conditional symmetric instability from atmospheric soundings. *Mon. Wea. Rev.*, **111,** 2016–2033.

——, 1988: Observational evidence of slantwise convective adjustment. *Mon. Wea. Rev.*, **116,** 1805–1816.

Ertel, H., 1942: Ein neuer hydrodynamischer Wirbelsatz. *Meteor. Z.*, **59,** 277–281.

Fritsch, J. M., and C. F. Chappell, 1980: Numerical prediction of convectively driven mesoscale pressure system. Part 1: Convective parameterization. *J. Atmos. Sci.*, **37,** 1722–1733.

Gilhousen, D. B., 1994: The value of NDBC observations during March 1993's "storm of the century." *Wea. Forecasting,* **9,** 255–264.

Gyakum, J. R., 1983a: On the evolution of the *QE II* storm. Part I: Synoptic aspects. *Mon. Wea. Rev.*, **111,** 1137–1155.

——, 1983b: On the evolution of the *QE II* storm. Part II: Dynamic and thermodynamic structure. *Mon. Wea. Rev.*, **111,** 1156–1173.

Hedley, M., and M. K. Yau, 1991: Anelastic modeling of explosive cyclogenesis. *J. Atmos. Sci.*, **48,** 711–727.

Hirschberg, P. A., and J. M. Fritsch, 1991: Tropopause undulations and development of extratropical cyclones. Part I: Overviews and observations from a cyclone event. *Mon. Wea. Rev.*, **119,** 496–517.

Hoskins, B. J., M. E. McIntyre, and A. W. Robertson, 1985: On the use and significance of isentropic potential vorticity maps. *Quart. J. Roy. Meteor. Soc.*, **111,** 877–946.

Juang, H.-M. H., and M. Kanamitsu, 1994: The NMC nested regional model. *Mon. Wea. Rev.*, **122,** 3–26.

Kuo, H. L., 1974: Further studies on the parameterization of the influence of cumulus convection on large-scale flow. *J. Atmos. Sci.*, **31,** 1232–1240.

Kuo, Y.-H., and S. Low-Nam, 1990: Prediction of nine explosive cyclones over the western Atlantic with a regional model. *Mon. Wea. Rev.*, **118,** 3–25.

——, and R. J. Reed, 1988: Numerical simulation of an explosively deepening cyclone in the eastern Pacific. *Mon. Wea. Rev.*, **116,** 2081–2105.

Mailhot, J., and R. Benoit, 1982: A finite-element model of the atmospheric boundary layer suitable for use with numerical weather prediction models. *J. Atmos. Sci.*, **39,** 2249–2266.

——, and C. Chouinard, 1989: Numerical forecasts of explosive winter storms: Sensitivity experiments with a meso-α scale model. *Mon. Wea. Rev.*, **117,** 1311–1343.

Reed, R. J., and M. D. Albright, 1986: A case study of explosive cyclogenesis in the eastern Pacific. *Mon. Wea. Rev.*, **114,** 2297–2319.

——, G. A. Grell, and Y.-H. Kuo, 1993: The ERICA IOP 5 storm. Part II: Sensitivity tests and further diagnosis based on model output. *Mon. Wea. Rev.*, **121,** 1595–1612.

Reuter, G. W., and M. K. Yau, 1990: Observations of slantwise convective instability in winter cyclones. *Mon. Wea. Rev.*, **118,** 447–458.

Roebber, P. J., 1990: Variability in successive operational model forecasts of maritime cyclogenesis. *Wea. Forecasting,* **5,** 586–595.

——, 1993: A diagnostic case study of self-development as an antecedent conditioning process in explosive cyclogenesis. *Mon. Wea. Rev.*, **121,** 976–1006.

——, J. R. Gyakum, and D. N. Trat, 1994: Coastal frontogenesis and precipitation during ERICA IOP 2. *Wea. Forecasting,* **9,** 21–44.

Rogers, R. R., W. L. Ecklund, D. A. Carter, K. S. Gage, and S. A. Ethier, 1993: Research applications of a boundary-layer wind profiler. *Bull. Amer. Meteor. Soc.*, **74,** 567–580.

Sanders, F., 1987: Skill of NMC operational dynamic models in the prediction of explosive cyclogenesis. *Wea. Forecasting,* **2,** 322–336.

——, and J. R. Gyakum, 1980: Synoptic–dynamic climatology of the "bomb." *Mon. Wea. Rev.*, **108,** 1589–1606.

——, and E. P. Auciello, 1989: Skill in prediction of explosive cyclogenesis over the western North Atlantic Ocean, 1987/1988: A forecast checklist and NMC dynamical models. *Wea. Forecasting,* **4,** 157–172.

Staniforth, A. N., and H. L. Mitchell, 1978: A variable-resolution finite element technique for regional forecasting with the primitive equations. *Mon. Wea. Rev.*, **106,** 439–447.

Tanguay, M., A. Simard, and A. N. Staniforth, 1989: A three-dimensional semi-Lagrangian scheme for the Canadian regional finite-element forecast model. *Mon. Wea. Rev.*, **117,** 1861–1871.

Uccellini, L. W., 1986: The possible influence of upstream upper-level baroclinic processes on the development of the *QE II* storm. *Mon. Wea. Rev.*, **111,** 1019–1027.

——, and D. R. Johnson, 1979: The coupling of upper- and lower-tropospheric jet streaks and implications for the development of severe convective storms. *Mon. Wea. Rev.*, **107,** 682–703.

——, and P. J. Kocin, 1987: The interaction of jet streak circulation during heavy snow events along the east coast of the United States. *Wea. Forecasting,* **2,** 289–308.

——, ——, R. A. Peterson, C. H. Wash, and K. F. Brill, 1984: The Presidents' Day cyclone of 18–19 February 1979: Synoptic overview and analysis of the subtropical jet structure influencing the pre-cyclogenetic period. *Mon. Wea. Rev.*, **112,** 31–55.

——, D. Keyser, K. F. Brill, and C. H. Wash, 1985: The Presidents' Day cyclone of 18–19 February 1979: Influence of a tropopause fold on rapid cyclogenesis. *Mon. Wea. Rev.*, **113,** 962–988.

——, R. A. Peterson, K. F. Brill, P. J. Kocin, and J. J. Tuccillo, 1987: Synergistic interactions between an upper-level jet structure and diabatic processes that influence the development of a low-level jet and a secondary coastal cyclone. *Mon. Wea. Rev.*, **115,** 2227–2261.

——, P. J. Kocin, and J. M. Sienkiewicz, 1994: Advances in forecasting extratropical cyclogenesis at the National Meteorological Center. Preprints, *Symp. on the Life Cycle of Extratropical Cyclones,* Bergen, Norway, Univ. of Bergen, 259–274.

Walker, N. D., 1993: A preliminary look at cyclogenesis in Gulf of Mexico during the March 1993 blizzard. *Mar. Wea. Log,* **37,** 8–9.

Wash, C. H., S. Heikkinen, C.-S. Liou, and W. A. Nuss, 1990: A rapid cyclogenesis event during GALE IOP 9. *Mon. Wea. Rev.*, **118,** 375–391.

Whitaker, J. S., L. W. Uccellini, and K. F. Brill, 1988: A model-based diagnostic study of the rapid development phase of the Presidents' Day cyclone. *Mon. Wea. Rev.*, **116,** 2337–2365.

Zhang, D.-L., 1989: The effect of parameterized ice microphysics on the simulation of vortex circulation with a mesoscale hydrostatic model. *Tellus,* **41A,** 132–147.